Presentation and discussion of the high resolution atmosphere-land surface-subsurface simulation dataset of the simulated Neckar catchment for the period 2007-2015

Bernd Schalge[1], Gabriele Baroni[2], Barbara Haese[3], Daniel Erdal[4], Gernot Geppert[5], Pablo Saavedra[1], Vincent Haefliger[1], Harry Vereecken[6,7], Sabine Attinger[8,9], Harald Kunstmann[3,10], Olaf A. Cirpka[4], Felix Ament[11], Stefan Kollet[6,7], Insa Neuweiler[12], Harrie-Jan Hendricks Franssen[6,7], Clemens Simmer[1,7]

[1]Institute for Geosciences, University of Bonn, Bonn, Germany

[2] Department of Agricultural and Food Sciences, University of Bologna, Bologna, Italy

[3]Institute of Geography, University of Augsburg, Augsburg, Germany

[4]Center for Applied Geoscience, University of Tübingen, Tübingen, Germany

[5]Department of Meteorology, University of Reading, Reading, England

[6]Forschungszentrum Jülich GmbH, Agrosphere (IBG-3), Jülich, Germany

[7]Centre for High-Performance Scientific Computing (HPSC-TerrSys), Geoverbund ABC/J, Jülich, Germany

[8]Institute of Earth and Environmental Science, University of Potsdam, Potsdam, Germany

[9]Helmholtz-Center for Environmental Research, Leipzig, Germany

[10]Institute of Meteorology and Climate Research (IMK-IFU), Karlsruhe Institute of Technology (KIT), Garmish-Partenkirchen, Germany

[11]Meteorological Institute, University of Hamburg, Hamburg, Germany

[12]Hannover, Institut für Strömungsmechanik und Umweltphysik im Bauwesen, Leibniz Universität Hannover, Germany

Correspondence to: Bernd Schalge (bschalge@uni-bonn.de)

Abstract.

Coupled numerical models, which simulate water and energy fluxes in the subsurface-land surface-atmosphere system in a physically consistent way are a prerequisite for the analysis and a better understanding of heat and matter exchange fluxes at compartmental boundaries and interdependencies of states across these boundaries. Complete state evolutions generated by such models may be regarded as a proxy of the real world, provided they are run at sufficiently high resolution and incorporate the most important processes. Such a simulated reality can be used to test hypotheses on the functioning of the coupled terrestrial system. Coupled simulation systems, however, face severe problems caused by the vastly different scales of the processes acting in and between the compartments of the terrestrial system, which also hinders comprehensive tests of their realism. We used the Terrestrial Systems Modeling Platform TerrSysMP, which couples the meteorological model COSMO, the land-surface model CLM, and the subsurface model ParFlow, to generate a simulated catchment for a regional

terrestrial system mimicking the Neckar catchment in southwest Germany. Simulations for this catchment are made for the period 2007-2015, and at a spatial resolution of 400m for the land surface and subsurface and 1.1km for the atmosphere. Among a discussion of modelling challenges, the model performance is evaluated based on observations covering several variables of the water cycle. We find that the simulated catchment behaves in many aspects quite close to observations of the real Neckar catchment, e.g. concerning atmospheric boundary-layer height, precipitation, and runoff. But also discrepancies become apparent, both in the ability of the model to correctly simulate some processes which still need improvement such as overland flow, and in the realism of some observation operators like the satellite based soil moisture sensors. The whole raw dataset is available for interested users. The dataset described here is available via the CERA database (Schalge et al, 2020): https://doi.org/10.26050/WDCC/Neckar_VCS_v1

1   Introduction

Earth environmental models are becoming increasingly important for climate and weather prediction, flood forecasting, water resources management, agriculture, and water quality control (e.g. Shrestha et al. 2014; Larsen et al. 2014; Simmer et al., 2015). Assuming that that the models are able to resemble the real-world based on state-of-the-art understanding of the system processes, the models are also used as "virtual realities" for hypothesis testing and decision support systems in many scientific disciplines (Clark et al., 2015, Semenova & Beven, 2015).

Virtual or simulated realities have been used for specific compartments of the terrestrial system in many studies (see Fatichi et al., 2016, and reference herein) and several advantages have been recognized. Bashford et al. (2002) computed simulated remote-sensing observations with 1 km resolution to derive, among others, process parameterizations for evapotranspiration in a hydrological model operating on the same scale as the remote sensing data. Weiler and McDonnel (2004) used a simulated-reality approach on the hill-slope scale to detect and quantify the major controls on subsurface flow processes and derive tunable parameters for conceptual models. Similar experiments allowed Schlueter et al. (2012) to explore the relationship between soil architecture and hydraulic behavior and Chaney et al. (2015) to testing sampling designs. Hein et al. (2019) explores the relative importance of different factors in the hydrologic response of a catchment. Simulated realities are also often used to overcome limitations on the data-scarce observations. In this context, Ajami and Sharma (2018) used simulations results to test disaggregation method for soil moisture observations. In subsurface hydrology it is a standard procedure to test inverse modeling and data-assimilation approaches on simulated aquifers (e.g., Zimmermann et al., 1998; Hendricks Franssen et al., 2009), which are used to generate realistic aquifer data with exactly known hydraulic and geochemical properties at every point (e.g., Schaefer et al., 2002).

More recently, it has been highlighted that the terrestrial systems should be better exploited by the use of integrated models which are able to simulate water and energy fluxes in the subsurface-land surface-atmosphere system in a physically consistent way (Clark et al., 2015, Davison et al, 2018). For this reason, these integrated modeling approaches have also

been considered to generate simulated realities (Mackay et al., 2015). However, despite the increasing computational capability and availability of infrastructures, these modelling approaches are generally more technically demanding. In addition, the use of these types of integrated models requires different expertises that are not usually cover within one single scientific group but requires strong interdisciplinary collaborations among different partners. For these reasons, the use of these types of models is still not commonly foreseen.

To overcome this limitation, in this paper we present the development, the testing and the data of a simulated reality of a mesoscale catchment based on a fully integrated terrestrial model system. Our simulated catchment encompasses the terrestrial system from the bedrock to the upper atmosphere covering the catchment of a higher-order river (length $\approx$ 380km, area $\approx$ 14000km^2) including a buffer zone surrounding it, in which we simulate - as realistically as currently possible - the multi-year evolution of states including the water and energy fluxes in and between all its compartments. We specifically venture to represent the strong spatial variability of the land components, which affects the overall system behavior due to nonlinear couplings and feedbacks. Since a simulated catchment with no resemblance to a real world catchment hardly allows for evaluating its realism, we base our simulation loosely on the Neckar catchment in southwest Germany that contains quite variable topography, different land cover, high and low precipitation regions, deep and shallow water tables and regions prone to flooding events. (see Figure 1). The model does not aim at exactly reproducing the catchment's response to hydro-climatic forcing, instead we only require that the simulated response is realistic with respect to typical spatial and temporal characteristics. For this reason, we discuss the model realism in comparison with observations of the real catchment, but also its limitations, particularly in relation to the chosen resolutions which balance the detail in process representation and computational feasibility.Despite these simplifications we believe this dataset will be useful in a variety of ways, such as data assimilation, model comparison studies and model development studies as well as focused impact studies. In the discussion section at the end we go more into detail how this dataset can potentially be used and what the limits of applicability are.

The remainder of the paper is structured as follows. In section 2, we introduce the simulation platform TerrSysMP, while Section 3 describes in detail the surface and subsurface parameters for topography, soils and aquifers, land use, vegetation, and the river network. In Section 4, we show snapshots and time series of state variables or system parameters extracted from the simulated catchment and compare them to observations in the real Neckar catchment to demonstrate how well the most important requirements are met. These results as well as possible ways to improve them are discussed in Section 5 together with several issues, which came up during the development phase. We provide conclusions and an outlook in Section 6.

2   The Terrestrial Systems Modeling Platform (TerrSysMP)

We used the Terrestrial System Modeling Platform (TerrSysMP, see Shrestha et al. 2014; Gasper et al. 2014; Sulis et al. 2015) developed within the Transregional Collaborative Research Centre TR32 (Simmer et al. 2015) for the generation of

96   the simulated catchment. TerrSysMP couples (Figure 1 in Gasper et al., 2014) the hydrologic flow model ParFlow v693

97   (Ashby and Falgout, 1996; Jones and Woodward, 2001; Kollet and Maxwell, 2006), the land-surface model Community

98   Land Model, CLM v3.5 (Oleson et al., 2008), and the atmospheric model Consortium for Small Scale Modeling (COSMO

99   v4.21, Baldauf et al., 2011) via the Ocean Atmosphere Sea Ice Coupling framework OASIS3 (e.g. Valcke et al., 2006), using

100   a dynamical two-way approach including down- and upscaling algorithms for fluxes and state variables between

101   computational grids of different resolution.

102   ParFlow is a variably saturated watershed flow model, which solves the three-dimensional Richards equation to model

103   saturated and unsaturated flow in the subsurface, and the fully integrated kinematic wave equation to model two-dimensional

104   overland flow. Also other global and regional hydrological models use the latter to route overland flow, e.g. MODCOU

105   (Haefliger et al., 2015) and TRIP (Alkama et al., 2012). Advanced Newton-Krylov multigrid solvers are used that are

106   especially suitable for massively parallel computer environments. Excellent model performance and parallel efficiency have

107   been documented by Jones and Woodward (2001), Kollet and Maxwell (2006), and Kollet et al. (2010). A unique feature of

108   ParFlow is the use of an advanced octree data structure for rendering overlapping objects in 3-D space, which facilitates

109   modeling complex geology and heterogeneity as well as the representation of topography based on digital elevation models

110   and watershed boundaries.

111   CLM is a single column biogeophysical land-surface model released by the National Center for Atmospheric Research

112   (NCAR), which considers coupled snow, soil, and vegetation processes. Land surface heterogeneity is represented as a

113   nested sub-grid hierarchy in which grid cells are composed of multiple land units (glacier, lake, wetland, urban, and

114   vegetation), snow/soil columns (to capture variability in snow and soil states within each land unit), and Plant Functional

115   Types (PFTs) to capture the biogeophysical and biogeochemical differences between broad categories of plants in terms of

116   their functional characteristics. In TerrSysMP, the 1-D Richards-equation model included in CLM is replaced by ParFlow.

117   COSMO is a limited-area, non-hydrostatic numerical weather prediction model, which operationally runs at the German

118   weather service DWD, among others, for Numerical Weather Prediction (NWP) and various scientific applications on the

119   meso-β and meso-γ scale. COSMO is based on the primitive thermo-hydrodynamical equations describing compressible

120   flow in a moist atmosphere. As a limited-area model, COSMO needs lateral boundary conditions from a driving larger-scale

121   model. We impose the lateral conditions by nesting COSMO in COSMO-DE which spans Germany. At the lateral

122   boundaries a relaxation technique is used in which the internal model solution is nudged against an externally specified

123   solution over a narrow transition zone between the two domains. Version 3.5 of CLM that is used here is already relatively

124   old. Even though version 5 was not yet available when we started our work, it is now and comparison is warranted. Newer

125   versions of CLM have several major improvements over 3.5. The first one is a more sophisticated routing scheme leading to

126   much improved soil moisture profiles. In our case we replace this part with ParFlow anyway so our older version is not a

127   disadvantage in that regard. Other improvements are the inclusion of carbon and nitrogen cycles as well as more options for

128   crop type vegetation. Here we purposely simplify our setup as we not only have and want static land use but also use a blend

129   type of crop with no sharp changes in LAI due to harvests. Instead, we assume harvest to be an ongoing process all

130 throughout autumn. Thus, all these improvements do not downgrade the simulation results presented and discussed in this
131 study.

132 Within OASIS3, the upscaling algorithm uses the mosaic or explicit sub-grid approach (Avissar and Pielke, 1989) in which
133 high-resolution land surface fluxes are averaged and transferred to the coarser resolution of the atmospheric model
134 component. The implemented Schomburg scheme (Schomburg et al., 2010, 2012) downscales atmospheric variables of the
135 lowest atmospheric model layer to the higher-resolved land surface model. The scheme involves (i) spline interpolation
136 while conserving mean and lateral gradients of the coarse field, (ii) deterministic downscaling rules to exploit empirical
137 relationships between atmospheric variables and surface variables, and (iii) the addition of high-resolution variability (i.e.
138 noise) in order to honor the non-deterministic part and to restore spatial variability.

139 TerrSysMP allows simulating the terrestrial water, energy, and biogeochemical cycles from the deeper subsurface including
140 groundwater (ParFlow) across the land-surface (CLM) into the atmosphere (COSMO). Water and energy cycles are coupled
141 via evaporation and plant transpiration; these processes are modeled by CLM with a non-linear coupling to ParFlow through
142 soil-water availability and root-water uptake (Figure 2). The two-way coupling between CLM and COSMO encompasses
143 radiation exchange and turbulent exchanges of moisture, energy, and momentum. OASIS3 allows for different temporal and
144 spatial resolutions of the coupled model components. For example, a temporal resolution of 15 minutes is sufficient for the
145 subsurface and land-surface components, whereas time steps as small as 5 seconds are needed for the atmosphere. A higher
146 spatial resolution can be assigned for the surface and subsurface parts to allow for a better representation of soil and land-use
147 heterogeneity.

148 Since high-resolution and long time-series of the fully coupled system are needed to satisfy our need to check the statistical
149 behavior of the system, the models were run on the IBM/BlueGeneQ System JUQUEEN at the Jülich Supercomputing
150 Centre (Jülich Supercomputing Centre, 2015). JUQUEEN has a total of 28672 nodes with 16 cores each. Our configuration
151 involved using 256 nodes for 12hours, restarting the simulation every 7 simulation days. This is necessary as the runtime for
152 Parflow can vary greatly depending on the conditions in the catchment. The total number of grid cells for the domain is
153 323,675 per model layer with 10 layers for CLM and 50 layers for ParFlow, and 58,420 grid-points for the 50 COSMO
154 layers resulting in 22.3 million grid cells. We ran the fully-coupled model for a total period of nine years (2007-2015) as
155 2007 was the first full year where high resolution atmospheric forcing was available and nine years was the maximum
156 possible length with our granted compute time. On average the actual runtime was approximately eight hours. This means
157 that for one year of simulation roughly 1.7 million core-hours are needed. For the full nine-year time-series that is about 12
158 million core-hours; another ~8 million hours were needed for the spin-up. We used an output interval of 15 minutes, which
159 results in a total output of 38.5TB of data for the full time-series, where about half was produced by COSMO and a quarter
160 each by CLM and ParFlow.

3   Description of the Simulated Catchment

Our simulated catchment is based on the Neckar catchment in southwestern Germany (see Figure 1), east of the Black Forest mountain range and north of the Jurassic ridge of the Swabian Alb. The catchment has a varying topography including mountains up to 1050 m a.s.l., river valleys, different land use types, i.e. grassland, cropland (majority of the area), broadleaf and needle leaf forest (see Figure 3), and relatively large soil spatial variability. Annual mean precipitation over the real catchment ranges between 500 and 2000mm (see Section 5.1) with highest values over the Black Forest. Inter-annual variability of precipitation can reach up to one third of the mean value. Monthly precipitation can vary largely and its mean annual cycle is weak with slightly lower values in spring and autumn. While summer precipitation is dominated by convection, winter precipitation is predominantly related to fronts of extra-tropical cyclones with enhanced precipitation over the mountains due to orographic lift. Daily average temperatures vary with altitude between -5°C and 0°C in January and between 13 and 18°C in July. Land use and cover in the lower elevations are dominated by agriculture while the Black Forest features mainly needle-leaf trees. Broad-leaf trees can be found over smaller areas throughout the catchment. The distance to groundwater is in large parts of the area restricted to a few meters, in particular in lowland areas, which assures strong coupling between groundwater table and evapotranspiration (Maxwell et al., 2007). These typical central European catchment features led us to choose the Neckar catchment as the basis for the simulated catchment.

The computational domain is a rectangular area of ~57,850km² encompassing the Neckar catchment of ~14,000km². The domain is larger than the Neckar catchment in order to allow the atmospheric model to develop its own internal dynamics. COSMO is run on a 1.1km horizonal grid with 230x254 grid points, which includes a 4 grid point-wide outer frame zone where only the lateral boundary forcing is used without coupling to the CLM, as well as 50 vertical layers in hybrid coordinates (terrain following at the surface, flat in the stratosphere). COSMO is set up identical to the operational COSMO-DE setup of the German national weather service (Deutscher Wetterdienst, DWD), e.g., the deep convection parameterization is switched off because at the chosen grid resolution convection is enabled by the dynamical core (see Section 2.1). In COSMO-DE, the operational resolution is 2.8km, so that the approximation regarding deep convection is even more appropriate in our simulations. Similar choices were taken by Smith et al. (2015), who simulated precipitation events of roughly the same domain using nested WRF models, where the cumulus parameterization was switched off at horizontal resolutions of 900m and 300m. Lateral boundary forcing and constant fields (topography, land-mask etc.) are provided by the COSMO-DE analysis fields, which are downscaled to the 1.1km grid by linear interpolation. The lateral relaxation zone, which moderates the jump from the lateral driving fields to the inner model area, is set to 12km.

A software restriction (unfixable bug specific to the system we were running on) does not allow for cases with more than 4.2 million CLM columns as the model does not initialize properly and crashes; thus, currently a higher spatial resolution for CLM and ParFlow than 400 m cannot be used for the Neckar catchment on the used system. So, ParFlow and CLM use the same horizontal grid with a resolution of 400 m and 535x605 grid points. The vertical grid for both component models is partially the same, with CLM limited to 10 vertical layers up to a total depth of 3 m shared with ParFlow, which has in total

194 50 vertical layers reaching down to 100m. COSMO runs with a 5sec timestep while CLM and Parflow run at 15min

195 timesteps, which is also the coupling frequency.

196 For setting up CLM, the European digital elevation model (DEM) by the European Environment Agency EEA

197 (http://www.eea.europa.eu/data-and-maps/data/eu-dem) was projected to the latitude/longitude grid and bi-linearly

198 interpolated to 400m from the original 30m spatial resolution. The same DEM is used to create the slope input files for

199 ParFlow. A slight modification to the original DEM was made in order to ensure that the simulated Neckar River would flow

200 in the correct valley, especially in the upper half of the catchment where the valley is not always properly resolved by the

201 400m resolution. In total, the elevation of 8 grid points was reduced to achieve proper routing for the Neckar River. The

202 resulting elevation map is part of the CLM input data and available with the dataset as supplementary material. We have not

203 considered rivers outside the Neckar catchment in these corrections; thus, there are cases where their routing is not identical

204 to the real rivers.

205 Land use is taken from the 2006 Corine Land Cover Data Set (http://www.eea.europa.eu/data-and-maps/data/corine-land-

206 cover-2006-raster-3) also provided by EEA. Since the latter dataset features many more land use types (at a resolution of

207 100m) than required by CLM, they were grouped according to the CLM (IGBP) Plant Functional Type classes (1) broad-leaf

208 forests, (2) needle-leaf forests, (3) grassland, (4) cropland, and (5) bare soil. Urban areas are not considered in this setup and

209 replaced by bare soil. Water surfaces (e.g., larger lakes like Lake Constance in the South of the domain) are also treated as

210 bare soil in CLM while COSMO uses its own land-mask and specific calculations for water surfaces. Therefore, no values

211 from CLM are used for water surfaces in COSMO. A few hundred grid cells feature shrubs (mostly areas that are re- or de-

212 forested or areas at higher altitudes) which are treated as forests, and each grid cell features only one – the most dominant –

213 plant functional type. The plant Leaf Area Index (LAI) is computed from MODIS (Myneni et al. 2002) as monthly averages

214 for the year 2008 for each of the four vegetated land use classes. As a result, interannual variability is not considered in this

215 simulation as we have the same LAI curve for each PFT each year. While this somewhat limits the comparability to ET

216 observations in spring it is somewhat lessend by the fact that CLM does always use the values from two months and

217 interpolates based on the date (for instance on the 1st of April the values from March and April would have almost equal

218 weight, while on the 14th of April the April weight is clearly dominant). This LAI is increased for all plant functional types

219 by 20 percent on average (exact change depending on PFT, more for forests, less for grassland and crops) in the summer

220 months and significantly changed from factors less than 1 to 3.3 in winter-time (DJF average, accounting for very little

221 changes in LAI for needle-leaf trees in that area) for needle-leaf forests in order to account for known biases in the MODIS

222 data (Tian et al. 2004) mostly related to snow cover and fractional land cover due to the satellite footprint. The stem area

223 index (SAI) is estimated from the LAI by a slightly modified (no dead leaves for crops, constant base SAI of 10 percent of

224 the maximum LAI) formulation of Lawrence and Chase (2007) and Zeng et al. (2002) to better represent European tree

225 types. Vegetation height was set to 7m for needle-leaf trees and 10m for broad-leaf trees to account for partial coverage by

226 shrubs, to 20 - 120cm for crops, and to 10 - 60 cm for grass depending on the time of the year with low values in the winter

227 months and largest values in July and August. Since we consider only one crop type, we do not specify a harvest date when
228 the plant height drops to its minimum, but assume a smooth decline between August and October.

229 For the representation of soils in CLM we use the 1:1,000,000 soil map (BUEK1000, roughly 1km resolution) provided by
230 the Federal Institute for Geosciences and Natural Resources - BGR
231 (http://www.bgr.bund.de/DE/Themen/Boden/Informationsgrundlagen/Bodenkundliche_Karten_Datenbanken/BUEK1000/
232 buek1000_node.html). This soil map is available for entire Germany; thus only small areas in Switzerland and France are
233 missing outside the Neckar catchment for which we assume a nearby soil class. BUEK1000 offers sand and clay percentages
234 as well as carbon content for two to seven soil horizons down to a maximum depth of 3m for each soil type. The carbon
235 content is used to infer soil color. For urban areas (modeled as bare soil, as mentioned above) a fixed soil color (class 8 in
236 CLM) was used.

237 Since soil properties may vary substantially at scales smaller than the 1km for which BUEK1000 is appropriate, which might
238 impact system dynamics (Binley et al. 1989, Herbst et al. 2006, Rawls 1983), the soil map is downscaled by artificially
239 adding variability using the conditional points method recently presented in Baroni et al. (2017) as follows:

240 (1)   The BUEK1000 soil map is randomly sampled at 1995 point locations with one sample every 5 km^2 on average, a
241 minimum sample distance of 250 m, and at least one sample for each soil type of the original soil map which is realistic in
242 the context of how soil maps are usually created. This strategy resulted from extensive testing by minimizing the tradeoffs
243 between reproducing the main features of the original soil map and creating variability at finer resolution.

244 (2)   The sample locations are used as conditional points for further interpolation. Here, texture, carbon content, and
245 depth of the first three soil horizons are extracted from the BUEK1000 resulting in variable soil depth rather than the
246 assumed unrealistic uniform soil depth. In addition, the sand content of the original map was increased by 20% (for clay-
247 rich areas that previously had practically no sand, less for areas that already had high sand content to avoid cases with >90%
248 sand) resulting in a slightly higher hydraulic conductivity because previous simulations yielded too shallow unsaturated
249 zones as was expected for the resoltion of this simulation. The change to sand content was a direct response to this issue as it
250 fixed most of the emerging biases

251 (3)   Experimental variograms and cross-variograms are calculated for all variables and exponential models were fitted
252 to all spatial structures.

253 (4)   A texture map (sand and clay percentage) is generated using a single realization based on conditional co-simulation
254 (Gomez-Hernandez and Journal, 1993) to provide the sub-scale variability (<1 km^2). Horizon depths and carbon content are,
255 however, assumed to have a smoothed spatial variability; therefore, they are interpolated based on ordinary kriging as the
256 removal of small-scale variability is not important for the depth and carbon content.

257 (5)   Since ParFlow describes retention and hydraulic conductivity curves based on van-Genuchten-Mualem parameters,
258 pedotransfer functions are applied to estimate these parameters. The pedotransfer functions of Cosby et al. (1984) ,is used to
259 estimate saturated hydraulic conductivity based on soil texture, the one from Rawls (1983) is used to estimate soil bulk
260 density based on soil texture and organic matter and the one from Tóth et al. (2015) is used to estimate van Genucthen

261 parameters based on soil texture and bulk density. These have been selected based on data availability, applicability of the

262 particular approaches, and previous evaluations conducted in the area (Tietje and Hennings, 1996).

263 In order to keep soil porosity identical between CLM and ParFlow, we replaced the porosity calculation within CLM (which

264 uses a different pedotransfer function). The Manning's surface roughness was set to a constant value of 5.52×10^{-4} h/m$^{1/3}$ and

265 the specific storage to 1×10^{-3}. The chosen surface roughness value results in a realistic base flow for the local rivers without

266 calibration. Repercussions of this choice are discussed in Chapter 6. Slopes of the main rivers are additionally smoothed to

267 avoid artificial ponded areas.

268 All these changes are part of the forcing files that are provided with the full dataset making it easy to reproduce our

269 simulations (https://cera-www.dkrz.de/WDCC/ui/cerasearch/entry?acronym=Neckar_VCS_v1_FORCING)

270 In order to allow for realistic flow in the saturated zone, the 3-D geologic model of the geological survey of the state of

271 Baden-Württemberg was used from which eleven rock types were defined for Baden-Württemberg (see Figure A1). Some

272 characteristic features of the domain, such as middle Triassic and Jurassic karst aquifers, are not included to avoid the

273 manifold hydrological challenges related to its modeling. While this can have significant impact on groundwater equilibrium

274 and dynamics on the decade time scale, for the rather short time period considered here we would simply be left with a bias.

275 For areas outside of Baden-Württemberg we extended the rock types at the boundary outwards to cover the full

276 computational domain. Tab. 1 summarizes porosity and hydraulic conductivity used in the domain for the different

277 stratigraphic units. Since karst features of limestones are not considered, porosities in stratigraphic units containing

278 limestones and crystalline rocks are set considerably higher than in nature to somewhat counter this.

279 Not covered by the discussed data sets (not part of the soil and not large enough to be resolved in the geological map) are the

280 large alluvial bodies filling large part of the Neckar valley throughout the domain (Riva et al., 2006). Up to 30% of the

281 runoff takes place in the subsurface especially during periods of base flow according to a sub-catchment simulation

282 performed for the year 2007. In that simulation we used measured precipitation and river discharge data together with the

283 simulated evapotranspiration to calculate the water balance over a whole year. While our simulated evapotranspiration rates

284 may be inaccurate, it is implausible that this can account for 30% of the precipitation as in this climate we are almost always

285 energy limited and therefore ET differences are reduced to LAI differences; i.e. the water could have left the domain only

286 through the subsurface. Thus, gravel channels are needed to account for this lateral flow. Since the valleys in the catchment

287 are often small compared to the limited horizontal resolution of the model, we conceptualize the alluvial bodies as gravel

288 layers underneath all river cells (cells with a mean pressure head >0.1m) and directly next to rivers (riverbanks, i.e., one grid

289 point besides each river cell). The assumed gravel layers reach from beneath the soil down to a depth of 8m. The gravel cells

290 are parameterized with a high hydraulic conductivity of 1 m/h, a porosity of 0.6 and van-Genuchten parameters of 2 for n

291 and 4m^{-1} for α (residual saturation is 0.06 cm^3/cm^3). Our setup results in a reasonable distribution of surface and subsurface

292 discharge at the outlet of the catchment and reasonable river – aquifer exchange fluxes. In addition to the gravel channels, we

293 included a layer of weathered bedrock, which starts below the soil and extents down to a depth of 6m. This layer is

294 characterized by substantially larger porosity (0.4) and hydraulic conductivity (0.1 m/h) than the rock below. This layer was

295 added to enhance subsurface flow and counter the common occurrence of too shallow water levels if these features are not
296 included. Both these changes are realistic when compared to the actual morphology of the Neckar river valley. While it is
297 quite narrow in many places, there are still significant alluvial deposits everywhere except the furthest upstream region
298 (which are not considered for this anyway due to the pressure cutoff). The choice for the weathered bedrock layer is also
299 reasonable given the temperature and moisture ranges leading to imperfections in the rock layers near the surface.

300 Since we enforce no-flow boundary conditions at the subsurface domain boundaries, all water has to eventually reach the
301 surface in order to leave the domain. This happens predominantly in areas outside of the Neckar catchment, e.g. in the upper
302 Rhine valley, thus soil-moisture values in this region may be too high.

303 **4   Results**

304 In the following, we present example results of the simulated-reality simulations in order to demonstrate its potential for a
305 better understanding of the dynamics in coupled terrestrial systems. We will also show that the simulations quite well
306 resemble observations in the real Neckar catchment, and thus can be used to develop and evaluate modelling and prediction
307 strategies. Precipitation is the strongest hydrological driver in this region; thus its realistic spatial and temporal variability in
308 the domain including its statistical relations with topography is important. Also, the state of the atmospheric boundary layer,
309 which reflects the interaction of the land surface with the atmosphere is a critical component of the terrestrial system, which
310 should be represented by the simulation with some confidence. Along with the comparisons we will also discuss the
311 challenges experienced with such a modeling setup.

312 Even though we do not aim to be as close to reality as possible, we feel it important to show that the model system is
313 behaving as expected and is thus suitable for the various use cases we discussed.Figure A2 shows as an example result a
314 snapshot of the simulated three-dimensional distribution of cloud water/ice, precipitation density, and volumetric soil
315 moisture. The soil exhibits different soil moisture layers, the variability of which is mainly connected to different soil
316 hydraulic properties. Only clouds reaching high enough to have sufficient cloud ice produce precipitation, and some
317 precipitation evaporates before it reaches the ground. Extended weather fronts moving through the domain (not shown),
318 which are imposed by the boundary conditions, are also simulated realistically (timing, strength of wind gusts, change of
319 wind direction, change in temperature and pressure) given the resolution of the atmospheric model.

320 **4.1   Relation between water table depth and evapotranspiration**

321 An important measure for hydro-meteorological interactions within a catchment is the relation between water availability
322 and surface energy flux partitioning. Thus, the simulated catchment simulation should capture the expected reduced
323 evapotranspiration (ET) with increasing distance to groundwater (e.g., Maxwell et al., 2007; Shrestha et al., 2014). In Figure
324 3, we show daily averaged evaporation (which here is equal to ET as all other contributors are zero) values over bare soil
325 against distance to groundwater for 30th April and 31st July for the year 2007. These days were chosen as they were preceded

with several dry days in almost the whole catchment leading to comparable states for the upper soil layers. April was almost completely dry (on average less than 3 mm precipitation over the domain), while July was much wetter, but the increased solar radiation and thus temperatures compared to April result in higher evaporation rates and thus a quicker drying of the top layer of the soil. Figure 3 indicates a reduction in evaporation when the distance to groundwater falls below 15 – 100cm, depending on soil properties with faster evaporation reduction for increasing soil sand contents. Such relations are less obvious for cells with significant plant cover: while trees show overall higher evaporation and almost no change with distance to groundwater due to their deep root zones, variability increases with larger distances to groundwater (not shown). Also crops and grassland show limited evaporation changes as a function of distance to groundwater, which can, however, be explained by the high water availability (no water stress) in the time period considered. Figure 3 also contains a small number of grid-points at water table depth of 7m or deeper with evaporation rates only slightly lower than in the shallow water table regions. These relate most likely to cells that retain high levels of upper-level soil moisture even during dry periods to support higher evaporation. This could be due to the way the water-table is calculated. We define the water-table as the deepest threshold between positive and negative pressure. Since there are some places where there is another saturated region closer to the surface, leading to higher water availability near the surface, the high value for water-table can be misleading with respect to near-surface soil moisture. Such a feature will only occur if the water-table is deep enough to begin with which is why we do not see this for water-tables of less than 10m.As a results volumetric soil moisture for these cells with deep water table but high evaporation is much more similar to cells with shallow water table than to cells with deep water table but low evaporation

We want to point out that in this region ET is almost always limited by atmospheric demand which is why we limit his analysis to bare-soil and evaporation only. Since the upper-most layers can dry quickly the resulting drop in evaporation can be seen which is not the case for ET if there is an extended root zone as we have even for crop and grassland. These bare-soil areas are not a feature of the real catchment and as such can not be compared to real measurements.

4.2 Precipitation

We compare the simulated precipitation with the 1x1 km gridded REGNIE product of DWD, derived from in-situ precipitation observations (Rauthe et al., 2013). For the evaluation of seasonal daily precipitation cycles hourly observations of 71 DWD observational stations are used. The simulated seasonal mean precipitation (Figure 5) and the annual mean precipitation (not shown) are governed by the orographic structures of the Black Forest and Swabian Alb. Values range between approximately 520 mm/year around Mannheim and 2105 mm/year over the Black Forest in good accordance with REGNIE concerning the overall pattern and range (510 mm/year – 2130 mm/year). Overall the simulation shows about 10% higher annual precipitation in the east and south and about 25% lower in the north and west compared to REGNIE. During winter (December to February) precipitation is dominated by advection from the west, which result in maxima over the upwind and peak zones of the mountains and leeward minima. The simulated winter pattern (j) compares well with REGNIE (k), but the model underestimates precipitation in the northwestern part of the catchment (l). Over the mountains a slight

lateral shift of this kind of precipitation pattern results in neighboring areas with under- and overestimation also found for COSMO simulations coupled to its own TERRA land surface model (e.g., Dierer et al., 2009; Lindau and Simmer, 2013). In fall, the difference pattern between simulations and REGNIE (i) is similar to the winter pattern, but has smaller contrasts. In spring, the simulated precipitation is higher compared to REGNIE. In the summer (June to August), cloud bases are usually higher and reduce the patterns caused by the luff-lee effects. Moist air extends further to the east and south and gets staunched by the alpine upland leading to enhanced precipitation there. The simulated summer precipitation pattern, which is dominated by convective precipitation, resembles the REGNIE pattern but exceeds the latter by about 20% lower over large parts of the catchment (Figure 4).

The mean seasonal diurnal precipitation cycles (Figure 5) reflect the dominating precipitation types. While observed and simulated winter precipitation (Figure 5b) do not show a diurnal cycle, summer precipitation (Figure 5a) increases over the afternoon reaching a maximum at about 7pm in accordance with the maximum of convective precipitation. The simulations reproduce this pattern but exhibit a weak second peak between 6am and 12am while the afternoon/evening increase is delayed by about two hours. The simulated daily precipitation distribution fits the observations especially in late afternoon and night while it overestimates precipitation during the late morning while underestimating it in early afternoon in summer. In Winter this effect is much less pronounced but still there. It is connected to convective showers that are still too small and parametrized. These parametrizations were not originally designed for the km scale and have issues at this resolution and start producing precipitation too early. While the simulated catchment has somewhat less dry and low precipitation days than REGNIE, the number of days between 4 and 10 mm are higher than in REGNIE (not shown). The simulated and observed seasonal precipitation cycles (Figure 6) compare very well and mean precipitation is nearly identical between simulations and observations. The model reproduces the seasonal cycle of maximum daily precipitation well, however with larger differences in the summer (see also Dierer et al. 2009).

4.3   Atmospheric State Variables and Surface Radiation

We compare the atmospheric boundary layer (ABL) of the simulated catchment to observations from the meteorological tower at Karlsruhe Institute of Technology (KIT; Kalthoff and Vogel, 1992) and with DWD radiosonde observations in Stuttgart (STG) (see Figure 1 for locations and Table A1 for details of observed quantities). To avoid a biased comparison due to land-cover mismatches between the simulation due to only having one land-use type per gridcell and the actual land use at the observation sites, the simulations are averaged over five-by-five atmospheric grid boxes centered around the observation sites thus giving approximately the same fractional land cover in both cases.

The 10m mean diurnal minimum temperatures in the catchment are between 0.5 K (January) and 2.5 K (August) higher than observed (Figure 7, top) and are reached approximately one hour later than observed with the subsequent morning temperature rise shifted accordingly. The simulated diurnal temperature maxima are on average 0.7 K lower than in the observations and are reached 30 minutes later than measured. The morning temperature gradient in the simulation ranges from 0.10 K/h in December to 0.31 K/h in April, which compares reasonably well with the observations (0.13/0.52 K/h in

January/April). The evening cooling, however, progresses too slowly and results in too high minimum temperatures. At 100 m above ground, diurnal maximum temperatures agree within 0.7 K while the warm bias of diurnal minimum temperatures (0.9 K) is smaller than at 10m height (Figure 7, bottom). Also at 100 m a 1h shift between the diurnal minimum temperatures and the morning temperature rise are found. In 200 m height, the simulated monthly mean diurnal cycles are practically identical to the KIT observations (not shown). The temperature standard deviations (mean absolute difference between daily and monthly mean profile) are somewhat smaller than observed, in particular during the afternoon for the summer half year when the reduction can be more than 20%.

COSMO in TerrSysMP estimates ABL heights via the bulk Richardson number criterion with a threshold of 0.22 for unstable and 0.33 for stable conditions (Szintai and Kaufmann, 2008). Both seasonal and diurnal variations of the mean ABL height at 0 and 12h local time agree well with the observations using the same criterion (Figure 8), but the simulation tends to overestimate ABL heights at nighttime by up to 150 m and underestimate it at daytime by up to 200 m in March. Figure 9 compares simulated mean vertical profiles of temperature, virtual potential temperature, and specific humidity with radiosonde observations at 0 h and 12 h local time in Stuttgart (STG) including the mean differences (bias) and the standard deviation of the differences. Simulations are up to 0.9 K warmer close to the surface at 0 h and up to 0.5 K colder at 12 h. At larger heights, the simulations are up to 0.5 K warmer depending on land cover. Specific humidity profiles at 0 h are approximately 0.2 g/kg too dry close to the surface and 0.2 g/kg too wet above 1500 m. At 12 h profiles are up to 0.3 g/kg too wet throughout. The simulations have smaller virtual potential temperature gradients and are thus less stable close to the surface at 0 h. At 12 h, the decreasing virtual potential temperature close to the surface is not captured and tends towards a more neutral instead of unstable profile at low heights.

At KIT (STG) the land surface receives on average 20 W/m^2 (5.3 W/m^2) more incoming shortwave radiation and 18 W/m^2 (8 W/m^2) less incoming longwave radiation indicating a somewhat lower cloud cover (or lower cloud optical depth) as observed. At daytime (6 h – 22 h), the mean outgoing longwave radiation matches the KIT observations, while at nighttime (22 h – 6 h) values are 7.2 W/m^2 larger than observed, which corresponds to a higher surface temperature of approximately 1.4 K.

Overall, the atmospheric profiles, including the ABL heights, are very close to observations during the day and at heights above 10m. Noteworthy differences only occur close to the surface with too high nighttime temperatures (up to 2.5 K in summer) and subsequently too small morning temperature gradients. Somewhat higher incoming shortwave and lower incoming longwave radiation at the surface indicate less cloud cover (or lower cloud optical depths) compared to the observations. These results are in line with a previous evaluation of a 2.2 km COSMO simulation (Ban et al. 2014). In addition, we note somewhat reduced unstable conditions at daytime close to the surface in the simulations.

4.4   Passive Microwave Observations

The most direct area-covering observations of soil moisture are currently provided by L-Band (1.4 GHz) passive microwave observations from satellites. The Community Microwave Emission Model (CMEM) is used as a forward operator to simulate

the brightness temperatures (TB) at this frequency in vertical and horizontal polarization (de Rosnay et al., 2009). CMEM simulates brightness temperatures at the top of the atmosphere resulting from microwave emission and interaction by soil, vegetation, and atmosphere based on the state variables of the simulated catchment. Input to CMEM are the percentages of clay and sand in the soil, the coverage with open water surfaces, the profiles of soil moisture and soil temperature, vegetation types, and leaf area index (LAI). Satellite orbit geometry, antenna pattern, foot-print and incidence angle are taken into account following the ESA SMOS (Soil Moisture Ocean Salinity) instrument specifications, i.e. a full-width-half-maximum field of view leading to a footprint of 40km across-orbit and 47km along-orbit at multiple incidence angles (Kerr 2001) is applied. This antenna pattern weighs the grid-cell simulated brightness temperatures (Figure 11, left) in order to obtain simulated SMOS observations. Finally, these synthetic observations are rendered according to pixels based on the Icosahedral Snyder Equal Area (ISEA) projection at a spatial separation of about 15 km similar to the SMOS L1C TB data product (Figure A4, right), which can then be compared with observations for an indirect evaluation of the simulation. Every pixel corresponds to a fixed geo-location of the real SMOS L1C data product over the modeled area. Optionally, the satellite observation operator in TerrSysMP is able to also replicate the NASA SMAP (Soil Moisture Active Passive) radiometer (Saavedra et al., 2016) for years beyond 2015 since when SMAP data is available.

We evaluate the simulated brightness temperature distribution over the domain with real SMOS observations between April 2011 and September 2011. The SMOS observations are corrected from radio-frequency interference (RFI) effects over the region following Saavedra et al. (2016). Initial results with CMEM adapted parameters for surface roughness and vegetation optical thickness (which needed to be increased from its standard values found in the literature), lead to a systematic underestimation of the brightness temperature of about -20K on average (see orange line in Figure A3, which compares real SMOS observations with the simulated brightness temperatures) and maximum and minimum differences of -33K and -6K, respectively, for an incidence angle of 30°. A similar underestimation of -14K resulted for the 40° incidence angle with maximum and minimum values of -34K and +15K (lower plot in Figure 10). Those differences are mainly caused by the too large near-surface soil moisture values in the simulated catchment. The cumulative distribution functions of the satellite-derived soil moisture products and the simulated soil moisture suggests an about 63% higher near-surface soil moisture compared to the satellite estimates (Saavedra et al. 2016, Figure 6) with extremes of 44% and 95%. With that, a daily matching of the cumulative distribution functions of the simulated catchment and satellite retrieved soil moisture are performed to find a factor which then is assumed to be the soil-moisture bias of the simulation and applied as a correction factor. Figure 10 compares true SMOS observations with simulated brightness temperatures obtained without and with day-to-day correction for the assumed soil-moisture bias of the simulation. The correction decreases the average bias in brightness temperature from -20K(-14K) to about -3K (-2K) for the incidence angle of 30° (40°) at horizontal polarization. Similar results are found when the simulations were statistically compared with observations of later years from the NASA SMAP (Fig. 3 in Saavedra et al. 2016). The remaining bias can probably be further reduced by fine tuning radiation interaction parameters in CMEM, and by including orographic effects on the effective incidence angle. These biases will be

458 addressed by an improved exploitation of the uncertainty of the radiation interaction parameters and by including in CMEM
459 a two-stream approximation to better simulate cases with dense vegetation in the future.

460 The microwave observations retrieved from the simulated catchment show a typical situation encountered in data
461 assimilation; more often than not there are biases between simulated and remote sensing observations. This discrepancy
462 usually has multiple causes, which can relate to the observations themselves, assumptions in the observation operator used to
463 simulate the observations, and in the model used to generate the systems state variables entering the observation operator.
464 Even if these differences cannot be removed, such observations can be highly valuable for data assimilation as long as
465 temporal tendencies are meaningful information. Usually, the bias is statistically corrected and thus only the information in
466 the temporal and (if meaningful) spatial variability of the observations is exploited for moving the model states towards the
467 true states.

4.5   Evaluation of River Discharge

469 We compare river discharge in the simulated catchment with observations made in the Neckar catchment at the gaging
470 stations Rockenau, Lauffen, and Plochingen for a three-year period from 2007 to 2009 (Figure 11). The range of the
471 hydrological response to precipitation in the simulated catchment is similar to the observations showing the same responses
472 to rain events as well as similar behavior during dry periods, which is noteworthy since no calibration to runoff data has been
473 applied to the model. The simulated discharge peaks are, however, higher and delayed by one to three days compared to the
474 observations. A reason could be a too large Manning´s coefficient and the model resolution. In the discussion we suggest a
475 scaling of Mannings coefficient to account for the mismatch between true river width and the model resolution in order to
476 better represent realistic flood dynamics. In spring and summer, the response to precipitation is significantly smoother than
477 observed and peak amplitudes vary with respect to peak amplitudes of the observations. The differences between observed
478 and simulated precipitation discussed above and the effects of the less predictable convective events during these seasons
479 may also play a significant role. Convective events will often be displaced in space and time compared to the observations
480 and may even show different individual life cycles including lifetime and amplitude. Finally, the base flow is much lower
481 compared to the real catchment during dry periods, most likely because the grid resolution is considerably larger than the
482 actual river width and the unresolved subsurface spatial heterogeneity. An increased hydraulic conductivity via an increased
483 soil sand content may reduce the base flow further as infiltration increases.
484 The results are further evaluated comparing the flow duration curve and the monthly run off coefficient. The former
485 represents the statistical probability to exceed a specific discharge value within a given time period while the latter is the
486 ratio between runoff and precipitation over the catchment area. Figure A4 shows the lower exceedance probability compared
487 to the observations, in particular for low discharge rates, a behavior attributed to the lower base flow component and
488 confirmed by the too low runoff coefficients in spring and summer but similar coefficients during the rest of the year (Figure

12). We hypothesize that in this period the simulation has a lower hydrological response also due to missing subsurface heterogeneity. As stated above, we have neglected karst features, which are known to produce fast lateral subsurface flows. Overall, the model captures the general statistical features of the catchment including the typical seasonal trends quite well, while differences are noted related to hydrological extremes and base flow. These differences could be reduced by model calibration from which we refrain because hydrological extremes are not primary the objective of this study. We discuss options to improve the representation of river discharge further below.

4.6   Groundwater

A plausibility check of the groundwater levels is performed in two steps. First, we visually inspect the groundwater depth map, shown in Figure 13a. Accordingly, the model shows a reasonable split between shallower and deeper (5 meter and below) groundwater tables compared to expected values from observations with shallower levels overall. Furthermore, the deeper sections are found in the mountainous areas of the model domain, which corresponds well with the real situation. It has to be noted though that regions with shallow groundwater levels often show very small values, likely not to be found in the real catchment where the unsaturated zone is usually thicker. In a second step, we compare simulated hydraulic heads with available data. The environmental protection agency of the state of Baden-Württemberg (Landesanstalt für Umwelt, Messungen und Naturschutz – LUBW) operates 33 continuous groundwater observation wells. Comparing those point measurements to simulation results of an uncalibrated model with 400m grid resolution makes little sense. Instead, we compare (1) the magnitude of the fluctuation (subtracting the yearly mean from the respective time series) in the groundwater table throughout the catchment during a year (calculated as the groundwater observation minus its mean, shown in Figure 13b) and (2) the average trend of the groundwater in the full model (calculated after subtracting the mean and scaling the fluctuations to have the same magnitude. According to Figure 13b, the magnitude of the groundwater fluctuations is within similar ranges as the observations (Figure 13b), while a few observation wells show larger magnitudes. Also, the fluctuations overall follow similar long-term patterns over the year (Figure 13c). Hence, the groundwater, given the coarse resolution of the model in comparison with the compared point measurements, shows a reasonable behavior.

5   Discussion

The size of the catchment and resolution considered (400 m) pose an enormous challenge in terms of required CPU-time. Still, the applicability of Darcy's law with laboratory-based parameters can be debated as we have to resort to apparent model parameters to produce realistic mass fluxes in the compartments. By compromising these technical and physical aspects in the setup of the simulated catchment, we experienced several challenges; three of them will be discussed which we believe to be inherent to simulating energy and mass fluxes across compartment boundaries with partial-differential-equation-based, high-resolution coupled models.

Representation of rivers and surface roughness: River flow in the ParFlow module of TerrSysMP is simulated by an overland flow module. Overland flow appears when hydraulic heads in the top cells are above the land surface. As there is no discrimination between overland flow and river flow, rivers in the simulation have the width of the grid resolution whereas the real rivers may be significantly narrower. Overland flow is represented in ParFlow with the kinematic wave approximation of the St. Venant equations with the surface friction parameterized by Manning's coefficient. Typical Manning's coefficients when assigned to e.g. to a 400 m grid cell while in fact the river is much narrower, would result in too high discharge values during rain events and far too low ones during dry periods. In both cases the always too low water levels caused by the too wide rivers result in a poor representation of river-subsurface exchange. Our current choice of Manning's coefficient in ParFlow (5.52×10^{-4} h/m$^{1/3}$) results in realistic average discharge throughout the year, albeit at too low flow velocities. In order to compensate for this inconsistency, the Manning's coefficient could be scaled such that the overland flow velocity in river cells equals the river flow velocity as proposed by Schalge et al. (2019), which improves the phasing between simulated and observed discharge and the discharge peak. Similarly, the hydraulic conductivity of the model top layer for river cells could be scaled in order to reduce the loss of too much surface water to the subsurface caused by the too wide river cells. These issues will become even more severe when model resolutions are reduced, e.g., for ensemble-based data assimilation because of the even higher demands for computing efficiency.

Coarsening of topography: The still coarse topography of the simulation reduces the true hill slopes where lateral flow on the surface and in the shallow subsurface takes place. This affects quick-flow components towards rivers. As shown by Shrestha et al. (2015), coarse topography directly impacts the storage of water in the unsaturated zone because drainage becomes less effective. This in turn can lead to an overestimation of latent and underestimation of sensible heat flux. Additionally, coarse-resolution model runs result in delayed and stretched discharge peaks in the rivers. The severity of this effect is proportional to the degree of topography smoothing, that is introduced by the coarser resolution; therefore, any change in subsurface parameters such as hydraulic conductivity will depend on the degree of coarsening and the location within a catchment. Especially in narrow valleys and in mountainous areas this will lead to an overestimation of soil moisture, which we have not yet compensated by changing other parameters. Recently a method has been proposed to improve these issues by scaling horizontal hydraulic conductivity (Foster and Maxwell, 2019).

Soil parameters: As outlined in section 2, the soil hydraulic parameters were generated based on soil maps of the real Neckar catchment. According to the maps, the soils in the catchment consist mainly of clay and silt, which have rather low saturated hydraulic conductivities and small air entry pressure values. In large areas of the domain, the water content in our first simulations was close to saturation, even for upper soil layers, and the infiltration velocities were unrealistically low. Reasons are the soil parameters, which do not capture the true soil heterogeneity; moreover, real infiltration often takes place in root channels, small fractures, and other small structures. Thus, infiltration is always underpredicted by models using observed soil parameters assuming homogeneity. Infiltration processes may be better captured with dual domain approaches, which are, however, computationally demanding. A workaround would be to change the soil hydraulic parameters in order to obtain stronger infiltration. Currently, we use an artificially increased sand percentage of the soils in order to stay consistent

with the concept of the pedotransfer functions used in CLM. We will also test known scaling rules (e.g., Ghanbarian et al., 2015) to increase for example the saturated hydraulic conductivity for larger soil units. These rules should be applied on the soil hydraulic parameters, estimated by the pedotransfer functions.

6   Conclusions and Outlook

In the present study we show the development and the data generated based on a integrated subsurface-land surface-atmosphere system TSMP. Plausibility tests for the derived simulated reality which tries to mimic the Neckar catchment in southwestern Germany, show that the simulated catchment is able to reproduce realistic behavior when compared to measurements. Comparisons of simulated precipitation and ABL statistics show a very reasonable agreement with observations. However, comparisons with observed passive microwave measurements by satellites shows clearly a systematic bias which is probably related to a mixture of systematic errors in the latter, assumptions in the used forward operator, parameterizations of land surface properties (soil parameters) in the simulation, and missing processes therein (e.g., preferential flow, hill-slope processes). The analysis also shows a realistic connection between evapotranspiration and distance to groundwater in the simulation, while larger deviations from reality are found for river discharge dynamics. The deficiencies could be traced to the model resolution, which limits the often much smaller river widths to multiples of the model resolution, and to the way river discharge is handled in the ParFlow component of TerrSysMP. A new parameterization scheme proposed by Schalge et al. (2019) will avoid such problems in future model simulations. The main issues we face for the upper Neckar are too high soil moisture and shallow groundwater levels. Several ideas have been proposed to improve the setup including scaling of the surface roughness and soil parameters in response to the results we obtained here. While these changes would show improvements, they are likely marginal or very specific (river discharge characteristics) and would therefore not warrant the great computational cost to re-run for such a long time. Future model developments of TerrSysMP may enable this option and it would be interesting to compare resulting datasets and quantify the simulation speed increase by using GPU compute technologies.

Overall the results are encouraging regarding the viability of the simulated reality as key input parameters to the land surface and subsurface show very good agreement with observations. For these reasons, the analysis show that the results can be used as a basis for the community for, among others, exploring feedbacks between compartments, identify in which conditions simplification of the models could be done (Baroni et al., 2019) or develop and test methods for assimilating observations across compartments . We encourage the scientific community to explore this data for the different applications. Within the study we also highlighted some limitations mainly due to the still sever technical limitation and the IT-requirements. We anticipate however that more sophisticated versions of simulated catchments (higher resolution, improved parameterization of sub-scale processes as discussed above) are already in progress that could be also compared to this dataset in further study.

584 Finally, we want to address the applicability and usefulness of this dataset for various studies. As indicated, this dataset can
585 be valuable for data assimilation both for testing new methods or algorithms and as a standard set for synthetic observations
586 to pull from. Due to the long timeseries we have covered almost any possible weather regime (with the exception of truly
587 extreme events) which can be a great advantage as some algorithms may work well for most conditions but may show
588 weaknesses for more specific ones (for instance CMEM and frozen soils). It also allows to investigate the impact of
589 simplifications such as using a fixed atmospheric forcing instead of a model and thus disregarding feedback mechanisms.
590 Next to data assimilation there are also model development and model analysis and comparison studies that can benefit from
591 this dataset. If specific changes to the model system are made, for example testing a new cloud parametrization, all of the
592 input files that are provided with this dataset can be used to quickly set up a working environment with known results to
593 compare to. Here the length of the simulation is again an advantage since any development can be tested for relevant time
594 slices. Going into detail on the analysis of this dataset with respect to compartment interactions may also be interesting. We
595 have shown the overall behavior of the system over but we have not studied specific interesting events in detail. There is
596 certainly still much to be learned here if time is available to further analyze it. One of these topics is considering more
597 transient changes (LAI and climate change) rather than the more static picture we present. Lastly, this setup can also be
598 considered as a template for ensemble-based setups in the future. Right now, reduced resolutions are needed in order to
599 sufficiently run many members of such a coupled model system. As we have shown, even this higher resolved simulation
600 still shows some biases that are directly related to resolution so increasing resolution also in ensembles will be logical step in
601 the future to obtain better results. When this happens, the methods we used here to generate this simulation will be very
602 useful as well as the analysis presented here to decide how an ensemble should be set up based on the goal (an ensemble for
603 flood forecasts would have very different focus than one for drought monitoring for example).

604

605 ## 7 Data Availability

606 The presented dataset is available in the CERA database of the German Climate Computing Center (DKRZ: Deutsches
607 Klimarechenzentrum GmbH) (Schalge et al., 2020) at https://doi.org/10.26050/WDCC/Neckar_VCS_v1. The full nine-year
608 time series (2007-2015) for all three compartments has a size of roughly 40TB in compressed netCDF4 format.
609 Nevertheless, we encourage the use of this data set for investigations on data assimilation, but also the general functioning of
610 catchments including cross-environmental interactions and predictability studies can profit from such complete state
611 evolutions of the regional Earth system.
612 The TerrSysMP model is built in a modular way and users are supposed to get the component models by themselves while
613 the coupling interface is provided through a git repository (https://git.meteo.uni-bonn.de). As of now, registration is required
614 to access the TerrSysMP git and wiki page.
615 Both ParFlow (https://parflow.org/) and CLM (http://www.cgd.ucar.edu/tss/clm/distribution/clm3.5/) are freely available for
616 download from their respective websites or repositories. COSMO is not available, but the DWD supplies it free of charge for
617 research purposes upon request. More information on this process can be found in the TerrSysMP wiki.

618

Acknowledgements

This research is funded by the Deutsche Forschungsgemeinschaft (DFG, FOR2131: "Data Assimilation for Improved Characterization of Fluxes across Compartmental Interfaces"). The authors gratefully acknowledge the Gauss Centre for Supercomputing e.V. (www.gauss-centre.eu) for funding this project by providing computing time through the John von Neumann Institute for Computing (NIC) on the GCS Supercomputer JUQUEEN at Jülich Supercomputing Centre (JSC). We thank the members of HPSC-TerrSys (http://www.hpsc-terrsys.de/hpsc-terrsys/EN/Home/home_node.html) and Klaus Goergen in particular for invaluable technical support with the JUQUEEN supercomputer. Furthermore, we thank Prabhakar Shresta and Mauro Sulis for their preliminary work and introduction to the TerrSysMP modeling platform. We also acknowledge work done on an earlier version of this script by Jehan Rihani.

References

Alkama, R., Papa, F., Faroux, S., Douville, H., and Prigent, C.: Global off-line evaluation of the ISBA–TRIP flood model, Climate Dyn., 38, 1389–1412, doi:10.1007/s00382-011-1054-9, 2012.

Ashby, S.F., and Falgout R. D.: A parallel multigrid preconditioned conjugate gradient algorithm for groundwater flow simulations, Nuclear Science and Engineering, 124(1), 145-159,1996.

Avissar, R., and Pielke, R. A.: A parameterization of heterogeneous land surfaces for atmospheric numerical models and its impact on regional meteorology. Monthly Weather Review, 117(10), 2113-2136, doi:10.1175/1520-0493(1989)117<2113:APOHLS>2.0.CO;2,1989.

Baldauf, M., Seifert, A., Foerstner, J., Majewski, D., Raschendorfer, M., and Reinhardt, T.: Operational convective-scale numerical weather prediction with the COSMO model: description and sensitivities. Monthly Weather Review, 139(12), 3887-3905, doi:10.1175/MWR-D-10-05013.1,2011.

Ban, N., Schmidli, J., and Schaer, C.: Evaluation of the convection-resolving regional climate modelling approach in decade-long simulations. J. Geophys. Res. Atmos., 119, 7889–7907, doi:10.1002/2014JD021478,2014.

Baroni, G., Schalge, B., Rakovec, O., Kumar, R., Schüler, L., Samaniego, L., Simmer, C., Attinger, S.: A comprehensive distributed hydrological modelling inter-comparison to support processes representation and data collection strategies. Water Resources Research. https://doi.org/10.1029/2018WR023941, 2019

Baroni, G., Zink, M., Kumar, R., Samaniego, L., Attinger, S.: Effects of uncertainty in soil properties on simulated hydrological states and fluxes at different spatio-temporal scales. Hydrol. Earth Syst. Sci. 21, 2301–2320. https://doi.org/10.5194/hess-21-2301-2017, 2017.

Bashford, K. E., Beven, K. J., and Young, P. C.: Observational data and scale-dependent parameterizations: explorations using a virtual hydrological reality. Hydrological Processes 16, 293–312. doi:10.1002/hyp.33,2002.

Binley, A., Elgy, J., and Beven, K.: A physically based model of heterogeneous hillslopes: 1. Runoff production. Water Resources Research, 25, 1219–1226. doi:10.1029/WR025i006p01219,1989.

Chan, S., Njoku, E., and Colliander, A.: SMAP L1C Radiometer Half-Orbit 36 km EASE-Grid Brightness Temperatures. Version 2. Boulder, Colorado USA: NASA National Snow and Ice Data Center Distributed Active Archive Center. doi:10.5067/Y9C3Q3060AZ5,2015.

Chaney, N. W., Roundy, J. K., Herrera-Estrada, J. E., and Wood, E. F. (2015): High-resolution modeling of the spatial heterogeneity of soil moisture: Applications in network design. Water Resources Research 51, 619–638. doi:10.1002/2013WR014964,2015.

Clark, M. P., Fan, Y., Lawrence, D. M., Adam, J. C., Bolster, D., Gochis, D. J., Hooper, R. P., Kumar, M., Leung, L. R., Mackay, D. S., Maxwell, R. M., Shen, C., Swenson, S. C. and Zeng, X.: Improving the representation of hydrologic processes in Earth system models. Water Resources Research, 51, 5929–5956. https://doi.org/10.1002/2015WR017096, 2015

Cosby, B. J., Hornberger, G. M., Clapp, R. B., and Ginn, T. R.: A Statistical Exploration of the Relationships of Soil Moisture Characteristics to the Physical Properties of Soils. Water Resour. Res., 0, 682–690. doi:10.1029/WR020i006p00682,1984.

de Rosnay, P., Drusch, M., Boone, A., Balsamo, G., Decharme, B., Harris, P., Kerr, Y., Pellarin, T., Polcher, J., and. Wigneron, J. P.: AMMA Land Surface Model Intercomparison Experiment coupled to the Community Microwave Emission Model: ALMIP-MEMP. Journal Geophysical Research, 114, D05108, doi:10.1029/2008JD010724,2009.

Davison, J.H., Hwang, H.-T., Sudicky, E.A., Mallia, D.V., Lin, J.C.: Full Coupling Between the Atmosphere, Surface, and Subsurface for Integrated Hydrologic Simulation. Journal of Advances in Modeling Earth Systems. https://doi.org/10.1002/2017MS001052, 2018

Dierer, S., Arpagaus, M., Seifert, A., Avgoustoglou, E., Dumitrache, R., Grazzini, F., Mercogliano, P., Milelli, M., and Starosta, K.: Deficiencies in quantitative precipitation forecasts: sensitivity studies using the COSMO model. Meteorologische Zeitschrift, 18 (6), 631-645, doi:10.1127/0941-2948/2009/0420,2009.

Foster, L.M., Maxwell, R.M., 2019. Sensitivity analysis of hydraulic conductivity and Manning's n parameters lead to new method to scale effective hydraulic conductivity across model resolutions. Hydrological Processes 33, 332–349. https://doi.org/10.1002/hyp.13327

Gasper, F., Goergen, K., Shrestha, P., Sulis, M., Rihani, J., Geimer, M., and Kollet, S.: Implementation and scaling of the fully coupled Terrestrial Systems Modeling Platform (TerrSysMP) in a massively parallel supercomputing environment-a case study on JUQUEEN (IBM Blue Gene/Q). Geoscientific model development discussions, 7, 3545-3573, doi:10.5194/gmdd-7-3545-2014,2014.

Gomez-Hernandez, J., Journel J., and Journel, A. G.: Joint Sequential Simulationof MultiGaussian Fields, in Troia '92, Amilcar Soares (Ed.), volume 1, pages 85-94, Kluwer Academic Publishers,1993.

682   Fatichi, S., Vivoni, E. R., Ogden, F. L., Ivanov, V. Y., Mirus, B., Gochis, D., Downer, C. W., Camporese, M., Davison, J.

683   H., Ebel, B., Jones, N., Kim, J., Mascaro, G., Niswonger, R., Restrepo, P., Rigon, R., Shen, C., Sulis, M., and Tarboton, D.:

684   An overview of current applications, challenges, and future trends in distributed process-based models in hydrology. J.

685   Hydrol. 537, 45–60. doi:10.1016/j.jhydrol.2016.03.026,2016.

686   Ghanbarian, B., Taslimitehrani, V., Dong,, G., and Pachepsky, Y. A.: Sample dimensions effect on prediction of soil water

687   retention curve and saturated hydraulic conductivity. Journal of Hydrology. 528,127-137,

688   doi:10.1016/j.jhydrol.2015.06.024,2015.

689   Haefliger, V., Martin, E., Boone, A., Habets, F., David, C. H., Garambois, P.-A., Roux, H., Ricci, S., Berthon, L., Thévenin,

690   A., and Biancamaria, S.: Evaluation of Regional-Scale River Depth Simulations Using Various Routing Schemes within a

691   Hydrometeorological   Modeling Framework for the Preparation of the SWOT Mission, Journal of Hydrometeorology,

692   16, 1821-1842, doi:10.1175/JHM-D-14-0107.1,2015.

693   Hein, A., Condon, L., Maxwell, R M.: Evaluating the relative importance of precipitation, temperature and land-cover

694   change in the hydrologic response to extreme meteorological drought conditions over the North American High Plains.

695   Hydrology and Earth System Sciences 23, 1931–1950. https://doi.org/10.5194/hess-23-1931-2019, 2019

696   Hendricks Franssen, H. J., Alcolea, A., Riva, M., Bakr, M., Van der Wiel, N., Stauffer, F., and Guadagnini, A.: A

697   comparison of seven methods for the inverse modelling of groundwater flow. Application to the characterisation of well

698   catchments, Adv. Water. Resour., 32 (6), 851-872, doi:10.1016/j.advwatres.2009.02.011,2009.

699   Herbst, M., Diekkrueger, B., and Vanderborght J.: Numerical experiments on the sensitivity of runoff generation to the

700   spatial variation of soil hydraulic properties. Journal of Hydrology, 326, 43–58. doi:10.1016/j.jhydrol.2005.10.036,2006.

701   Jones, J. E., and Woodward C. S.: Newton–Krylov-multigrid solvers for large-scale, highly heterogeneous, variably

702   saturated flow problems. Advances in Water Resources, 24(7), 763-774, 2001.

703   Jülich Supercomputing Centre. JUQUEEN: IBM Blue Gene/Q Supercomputer System at the Jülich Supercomputing Centre.

704   Journal of large-scale research facilities, 1, A1. doi:10.17815/jlsrf-1-18, 2015.

705   Kalthoff, N., and Vogel, B.: Counter-current and channelling effect under stable stratification in the area of Karlsruhe.

706   Theor. Appl. Climatol., 45(2), 113-126, doi:10.1007/BF00866400,1992.

707   Kerr, Y H, Waldteufel, P, Wigneron, J P, Front, J and Berger, M: Soil moisture retrieval from space: The soil moisture and

708   ocean salinity (SMOS) mission. IEEE Trans. Geosci. Re. Sens., 39(8): 1729–1735. DOI:https://doi.org/10.1109/36.942551,

709   2001.

710   Kollet, S. J., and Maxwell, R. M.: Integrated surface–groundwater flow modeling: A free-surface overland flow boundary

711   condition in a parallel groundwater flow model. Advances in Water Resources, 29(7), 945-958,

712   doi:10.1016/j.advwatres.2005.08.006,2006.

713   Kollet, S. J., Maxwell, R. M., Woodward, C. S., Smith, S., Vanderborght, J., Vereecken, H., and Simmer, C.: Proof of

714   concept of regional scale hydrologic simulations at hydrologic resolution utilizing massively parallel computer resources.

715   Water Resources Research, 46(4), doi:10.1029/2009WR008730,2010.

Kurtz, W., He, G., Kollet, S. J., Maxwell, R. M., Vereecken, H., and H. Franssen, H.-J.: TerrSysMP-PDAF version 1.0): a modular high-performance data assimilation framework for an integrated land surface-subsurface model. Geoscientific Model Development, 9(4), 1341-1360, doi:10.5194/gmd-9-1341-2016,2016.

Larsen, M. A. D., Refsgaard, J. C., Drews, M., Butts, M. B., Jensen, K. H., Christensen, J. H., and Christensen, O. B.: Results from a full coupling of the HIRHAM regional climate model and the MIKE SHE hydrological model for a Danish catchment, Hydrol. Earth Syst. Sci., 18, 4733-4749, doi:10.5194/hess-18-4733-2014, 2014.

Lawrence, P. J., and Chase, T. N.: Representing a new MODIS consistent land surface in the Community Land Model (CLM 3.0). J. Geophys. Res., 112, G01023, doi:10.1029/2006JG000168,2007.

Lindau, R., and Simmer C.: On correcting precipitation as simulated by the regional climate model COSMO-CLM with daily rain gauge observations. Meteorology and Atmospheric Physics, 119, 1-2, p.31-42, doi:10.1007/s00703-012-0215-7,2013.

Mackay, E. B., Wilkinson, M. E., Macleod, C. J. A., Beven, K., Percy, B. J., Macklin, M. G., Quinn, P. F., Stutter, M., and Haygarth, P. M.: Digital catchment observatories: A platform for engagement and knowledge exchange between catchment scientists, policy makers, and local communities. Water Resour. Res., 51(6), 4815-4822. doi:10.1002/2014WR016824,2015.

Maxwell R. M., Chow F. K., Kollet S. J.: The groundwater-land-surface-atmosphere connection: Soil moisture effects on the atmospheric boundary layer in fully-coupled simulations, Advances in Water Resour., 30(12), 2447-2466, 2007

Myneni, R. B., Hoffman, S., Knyazikhin, Y., Privette, J. L., Glassy, J., Tian, Y., Wang, Y., Song, X., Zhang, Y., Smith, G. R., Lotsch, A., Friedl, M., Morisette, J. T., Votava, P., Nemani, R. R., and Running, S. W.: Global products of vegetation leaf area and fraction absorbed PAR from year one of MODIS data. Remote Sensing of Environment, 83(1), 214-231, doi:10.1016/S0034-4257(02)00074-3,2002.

Oleson, K. W., Niu, G. Y., Yang, Z. L., Lawrence, D. M., Thornton, P. E., Lawrence, P. J., and Qian, T.: Improvements to the community land model and their impact on the hydrological cycle. Journal of Geophysical Research: Biogeosciences (2005–2012), 113(G1), doi:10.1029/2007JG000563,2008.

Poltoradnev, M., Ingwersen, J., and Streck, T.: Spatial and temporal variability of soil water content in two regions of Southwest Germany during a three-year observation period. Vadose Zone Journal, 15(6), doi:10.2136/vzj2015.11.0143,2016.

Rauthe, M., Steiner, H., Riediger, U., Mazurkiewicz, A., and Gratzki, A. (2013): A Central European precipitation climatology – Part I: Generation and validation of a high-resolution gridded daily data set (HYRAS), Vol. 22(3), p 235–256, doi:10.1127/0941- 2948/2013/0436,2013.

Rawls, W. J.: Estimating soil bulk density from particle size analysis and organic matter content. Soil Sci., 135 (2), 123-125,1983.

Ridler, M. E., van Velzen, N., Hummel, S., Sandholt, I., Falk, A. K., Heemink, A., and Madsen, H.: Data assimilation framework: linking an open data assimilation library (OpenDA) to a widely adopted model interface (OpenMI), Environ. Modell. Softw., 57, 76–89, doi:10.1016/j.envsoft.2014.02.008, 2014.

749   Riva, M., Guadagnini, L., Guadagnini, A., Ptak, T., and Martac, E. (2006): Probabilistic study of well capture zones

750   distribution at the Lauswiesen field site. J. Contam. Hydrol. 88, 92–118, doi:10.1016/j.jconhyd.2006.06.005,2006.

751   Saavedra P., Simmer, C., and Schalge, B.: Evaluation of modeled high resolution soil moisture virtual brightness

752   temperature compared to space-borne observations for the Neckar catchment. IEEE Xplore 14th Specialist Meeting on

753   Microwave   Radiometry   and   Remote   Sensing   of   the   Environment   (MicroRad),   pp.   85-90,

754   doi:10.1109/MICRORAD.2016.7530510,2016.

755   Saavedra, P. and Simmer, C.: An Octave/MATLAB® Interface for Rapid Processing of SMOS L1C Full Polarization

756   Brightness Temperature. Journal of Open Research Software, 6, 1, p.2, DOI: http://doi.org/10.5334/jors.165, 2018

757   Schaefer, D., Dahmke, A., Kolditz, O., and Teutsch, G.: Virtual Aquifers: A Concept for Evaluation of Exploration,

758   Remediation and Monitoring Strategies. In: Calibration and Reliability in Groundwater Modelling: A Few Steps Closer to

759   Reality (Proceedings of the ModelCARE 2002 Conference held in Prague, Czech Republic, June 2002), edited by K. Kovar,

760   Z. Hrkal, IAHS Publication 277, IAHS Press Oxfordshire, pp. 52-59,2002.

761   Schalge, B., Haeflinger, V, Kollet, S, and Simmer, C: Improvement of surface runoff in the hydrological model ParFlow by

762   a scale-consistent river parameterization. Accepted for publication in Hydrological Processes, 2019.

763   Schalge, Bernd; Baroni, Gabriele; Haese, Barbara; Erdal, Daniel; Geppert, Gernot; Saavedra, Pablo; Haefliger, Vincent;

764   Vereecken, Harry; Attinger, Sabine; Kunstmann, Harald; Cirpka, Olaf A.; Ament, Felix; Kollet, Stefan; Neuweiler, Insa;

765   Hendricks Franssen, Harrie-Jan; Simmer, Clemens (2020). Virtual catchment simulation based on the Neckar region. World

766   Data Center for Climate (WDCC) at DKRZ. https://doi.org/10.26050/WDCC/Neckar_VCS_v1

767   Schlueter, S., Vogel, H.-J., Ippisch, O., Bastian, P., Roth, K., Schelle, H., Durner, W., Kasteel, R., and Vanderborght, J.:

768   Virtual soils: assessment of the effects of soil structure on the hydraulic behavior of cultivated soils. Vadose Zone Journal

769   11, doi:10.2136/vzj2011.0174,2012.

770   Schomburg, A., Venema, V., Lindau, R., Ament, F., and Simmer, C.: A downscaling scheme for atmospheric variables to

771   drive soil–vegetation–atmosphere transfer models. Tellus B, 62(4), 242-258, doi:10.1111/j.1600-0889.2010.00466.x,2010.

772   Schomburg, A., Venema, V., Ament, F., and Simmer, C.: Disaggregation of screen-level variables in a numerical weather

773   prediction model with an explicit simulation of subgrid-scale land-surface heterogeneity. Meteorology and Atmospheric

774   Physics, 116(3-4), 81-94, doi:10.1007/s00703-012-0183-y,2012.

775   Semenova, O., and Beven, K.: Barriers to progress in distributed hydrological modelling: Invited commentary. Hydrological

776   Processes, 29(8), 2074–2078. https://doi.org/10.1002/hyp.10434

777   Shi, Y., Davis, K. J., Zhang, F., Duffy, C. J., and Yu, X.: Parameter estimation of a physically based land surface hydrologic

778   model using the ensemble Kalman filter : A synthetic experiment, Water Resources Research, 50(1), 706-724,

779   doi:10.1002/2013wr014070,2014.

780   Shi, Y., Davis, K. J., Zhang, F., Duffy, C. J., and Yu, X.: Parameter estimation of a physically-based land surface hydrologic

781   model using an ensemble Kalman filter: A multivariate real-data experiment, Advances in Water Resources, 83, 421-427,

782   doi:10.1016/j.advwatres.2015.06.009,2015.

Shrestha, P., Sulis,, M., Masbou, M., Kollet, S., and Simmer, C.: A scale-consistent terrestrial systems modeling platform based on COSMO, CLM, and ParFlow. Monthly Weather Review, 142(9), 3466-3483, doi:10.1175/MWR-D-14-00029.1,2014.

Shrestha, P., Sulis, M., Simmer, C., Kollet, S.: Impacts of grid resolution on surface energy fluxes simulated with an integrated surface-groundwater flow model, Hydrol. Earth Syst. Sci., 19, 4317-4326, doi:10.5194/hess-19-4317-2015,2015.

Simmer, C., Thiele-Eich, I., Masbou, M., Amelung, W., Crewell, S., Diekkrueger, B., Ewert, F., Hendricks Franssen, H.-J., Huisman, A. J., Kemna, A., Klitzsch; N., Kollet, S., Langensiepen, M., Loehnert, U., Rahman, M., Rascher, U., Schneider, K., Schween, J., Shao, Y., Shrestha, P., Stiebler, M., Sulis, M., Vanderborght, J., Vereecken, H., van der Kruk, J., Zerenner, T., and Waldhoff, G.: Monitoring and Modeling the Terrestrial System from Pores to Catchments - the Transregional Collaborative Research Center on Patterns in the Soil-Vegetation-Atmosphere System. Bulletin of the American Meteorological Society, 96, 1765–1787. doi:10.1175/BAMS-D-13-00134.1,2015.

Smith, V. H., Mobbs, S. D., Burton, R. R., Hobby, M., Aoshima, F., Wulfmeyer, V., and Di Girolamo, P.: The role of orography in the regeneration of convection: A case study from the convective and orographically-induced precipitation study. Meteorologische Zeitschrift, Vol. 24, No. 1, 83–97, doi:10.1127/metz/2014/0418,2015.

Sulis, M., Langensiepen, M., Shrestha, P., Schickling, A., Simmer, C., and Kollet, S. J.: Evaluating the influence of plant-specific physiological parameterizations on the partitioning of land surface energy fluxes. Journal of Hydrometeorology, 16(2), 517-533, doi:10.1175/JHM-D-14-0153.1,2015.

Szintai, B., and Kaufmann , P.: TKE as a measure of turbulence. COSMO Newsletter 8, 2-9,2008.

Tian, Y., Dickinson, R. E., Zhou, L., Zeng, X., Dai, Y., Myneni, R. B., Knyazikhin, Y., Zhang, X., Friedl, M., Yu, I., Wu, W., and Shaikh, M.: Comparison of seasonal and spatial variations of leaf area index and fraction of absorbed photosynthetically active radiation from Moderate Resolution Imaging Spectroradiometer (MODIS) and Common Land Model. J. Geophys. Res., 109, D01103, doi:10.1029/2003JD003777,2004.

Tietje, O., and Hennings, V.: Accuracy of the saturated hydraulic conductivity prediction by pedo-transfer functions compared to the variability within FAO textural classes. Geoderma, 69, 71–84. doi:10.1016/0016-7061(95)00050-X,1996.

Tóth, B., Weynants, M., Nemes, A., Makó, A., Bilas, G., and Tóth, G.: New generation of hydraulic pedotransfer functions for Europe: New hydraulic pedotransfer functions for Europe. Eur. J. Soil Sci., 66, 226–238. doi:10.1111/ejss.12192,2015.

Valcke, S.: OASIS3 PRISM Model Interface Library: OASIS3 User Guide. PRIMS Support Initiative, Report No. 3,2006.

Weiler, M., and McDonnell, J.: Virtual experiments: a new approach for improving process conceptualization in hillslope hydrology. Journal of Hydrology 285, 3–18. doi:10.1016/S0022-1694(03)00271-3,2004.

Zeng, X., Shaikh, M., Dai, Y., Dickinson, R. E., Myneni, R.: Coupling of the common land model to the NCAR community climate model. J. Climate 15, 1832–1854, doi:10.1175/1520-0442(2002)015<1832:COTCLM>2.0.CO;2,2002.

Zimmerman, D. A., G. de Marsily, G., C.A. Gotway, C. A., M.G. Marietta, M. G., C.L. Axness, C. L., R.L. Beauheim, R. L., Bras, R. L., Carrera, J., Dagan, G., Davies, P. B., Gallegos, D. P., Galli, A., Gomez-Hernandez, J., Grindrod, P., Gutjahr, A. L., Kitanidis, P. K., Lavenue, A. M., McLaughlin, D., Neuman, S. P., RamaRao, B. S., Ravenne, C., and Rubin, Y.: A

817   comparison of seven geostatistically based inverse approaches to estimate transmissivities for modeling advective transport

818   by groundwater flow, Water Resour Res 34(6), 1373-1413, doi:10.1029/98WR00003,1998.

819
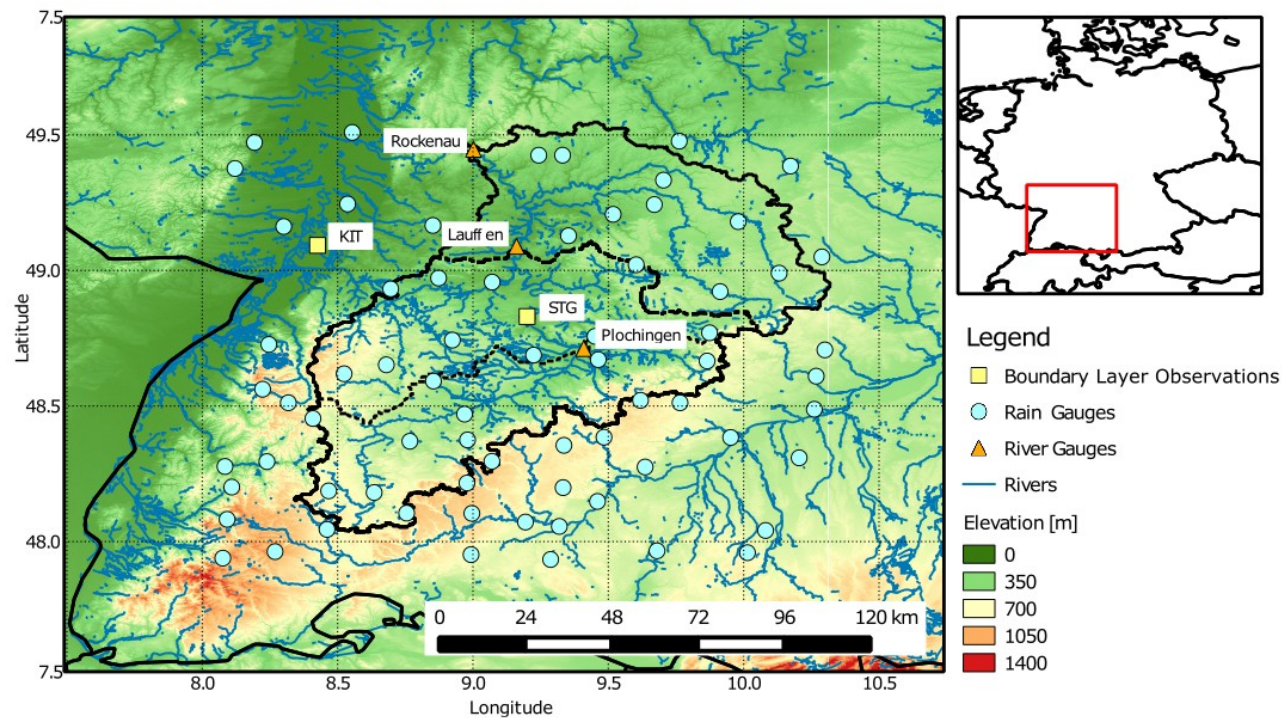
820

821   **Figure 1: Location of the Neckar catchment within SW Germany.**

822

823
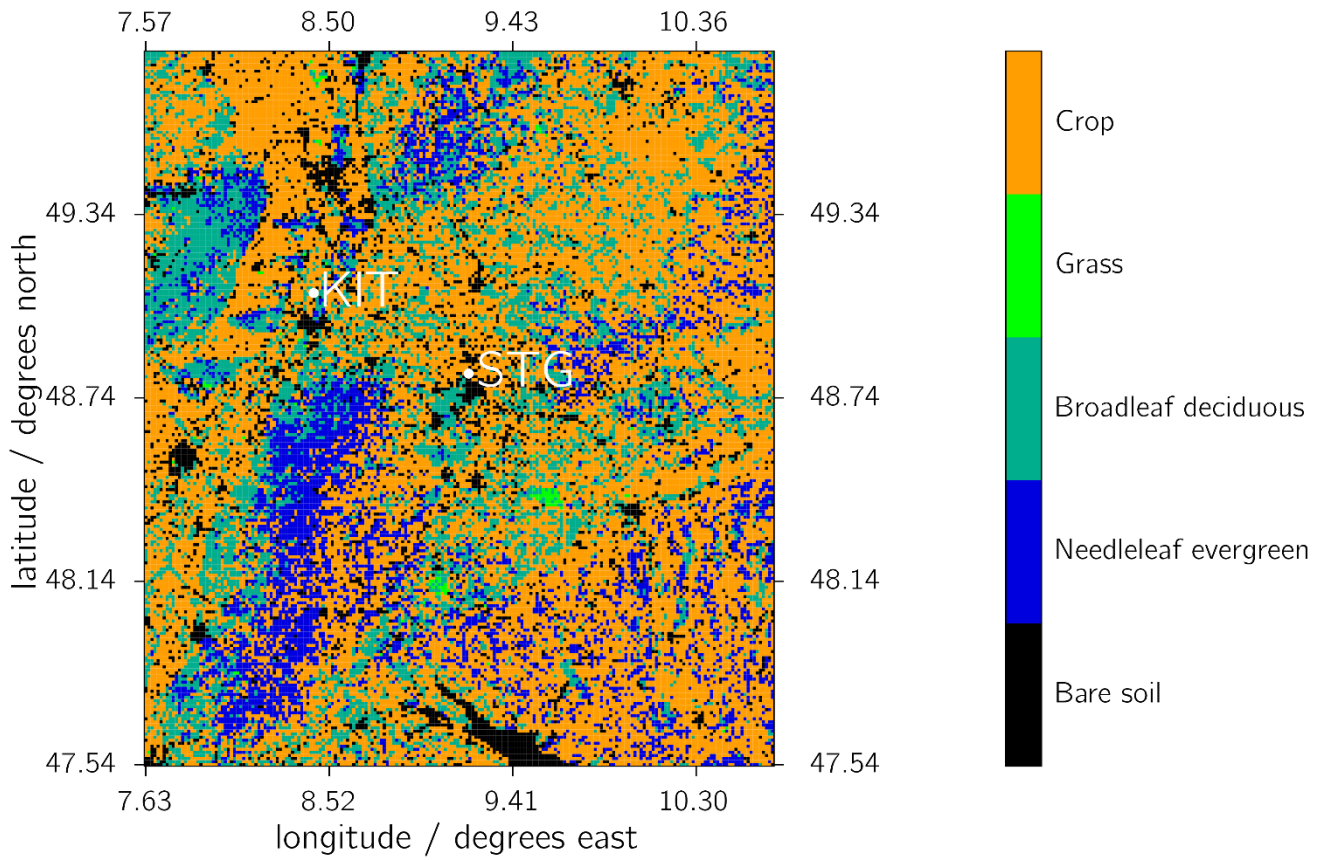
824 **Figure 2: Land cover in the simulated domain covering the entire Neckar catchment and bounding areas. KIT: Karlsruhe**
825 **Institute of Technology (location of meteorological tower observations), STG: Stuttgart (location of radiosonde observations).**

826

827
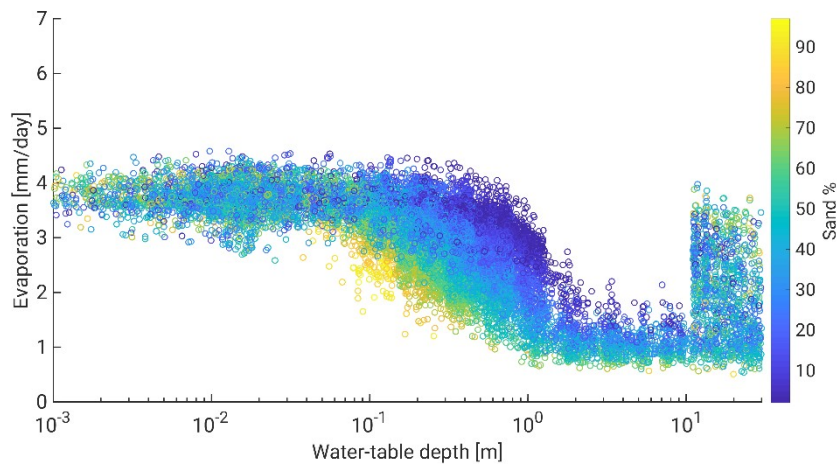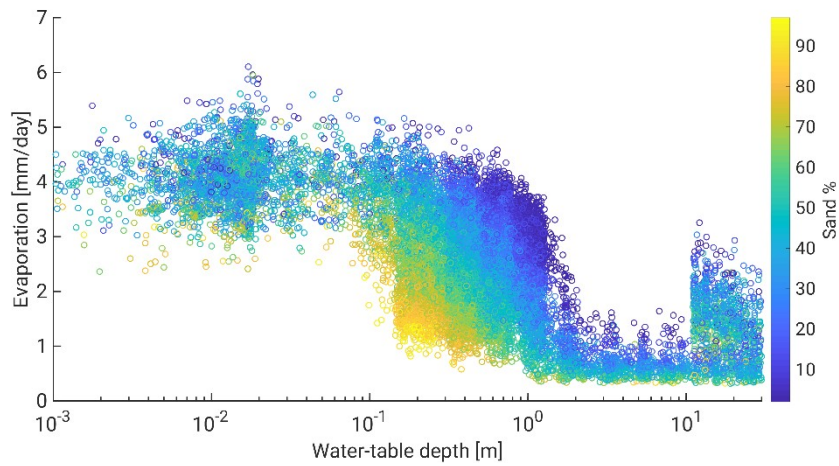
828 **Figure 3: Daily average evaporation simulated for 30th April (left) and 31st July 2007 in [mm/day]. The color indicates soil sand**
829 **percentage.**

830

831
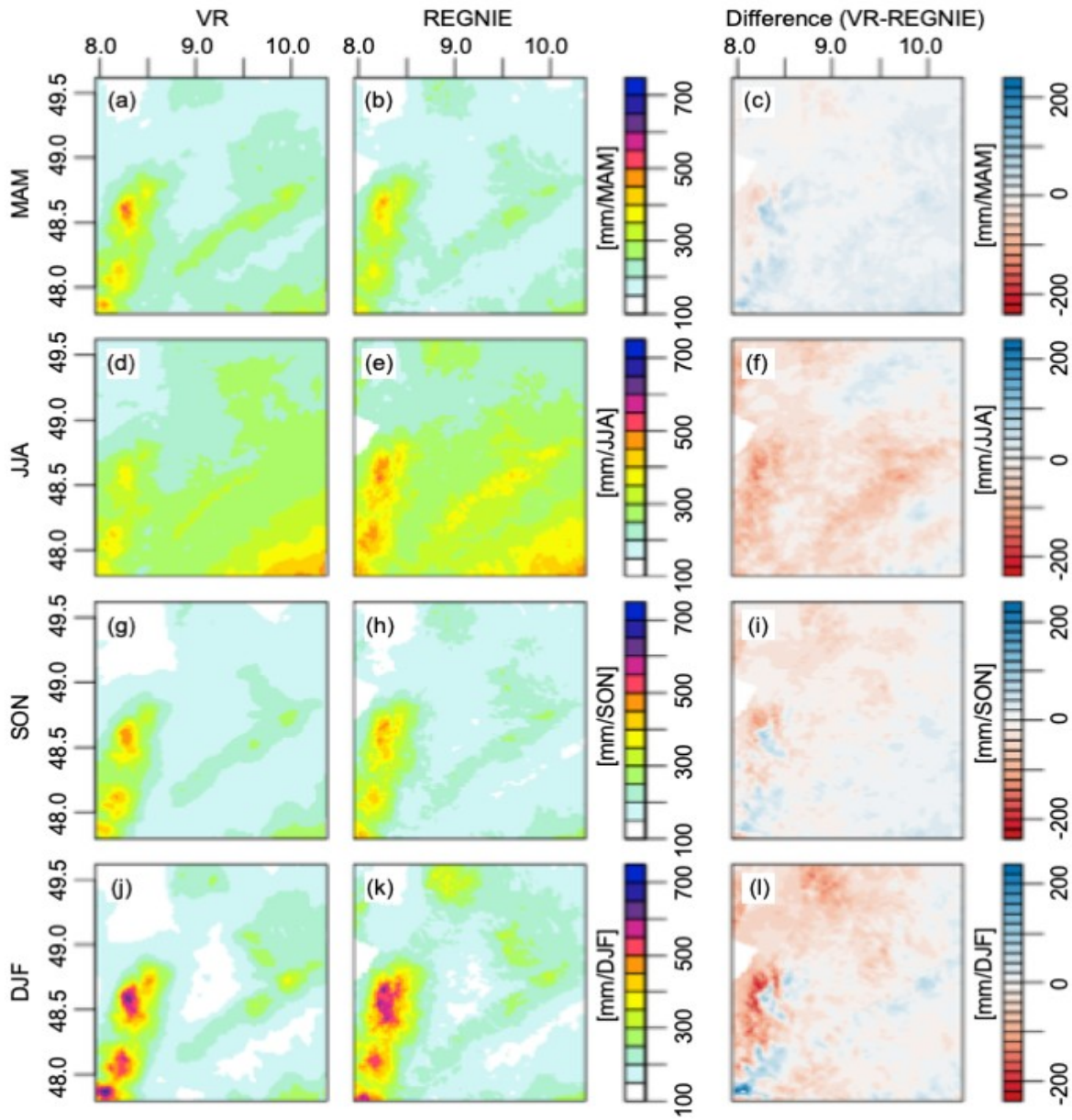
Figure 4: Mean seasonal precipitation over the Neckar catchment between 2007-2013 in the simulated reality (VR, left column) compared to the REGNIE data set (middle column). The difference between VR and REGNIE is shown in the right column. Figure (a), (b), and (c) show the comparison for spring (March – May); (d), (e), and (f) for summer (June – August); (g), (h), and (i) for fall (September – November); and (j), (k), and (l) for winter (December-February).

836

837

838
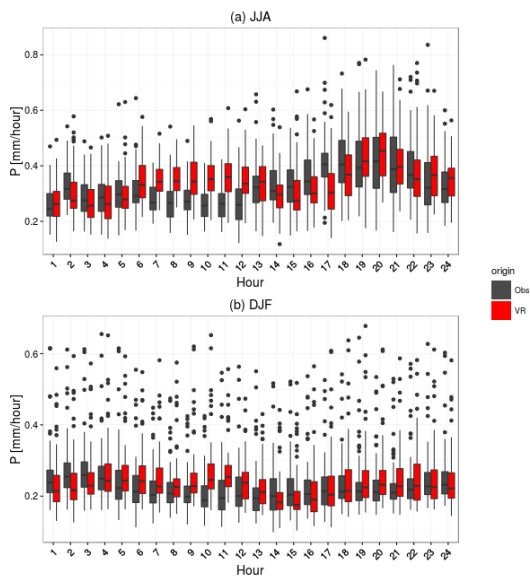
839 **Figure 5: Mean diurnal precipitation cycle for the 71 DWD stations and the corresponding simulations for wet days (more than 1**
840 **[mm/day]) for June-August (a) and December-February (b) season. The upper and lower hinges correspond to the first and third**
841 **quartile, the center black line the median, the upper whisker (analog for lower whisker) extends from the hinge to the highest**
842 **value within 1.5*(interquartile range), and the black dots mark the outliers.**

843

844
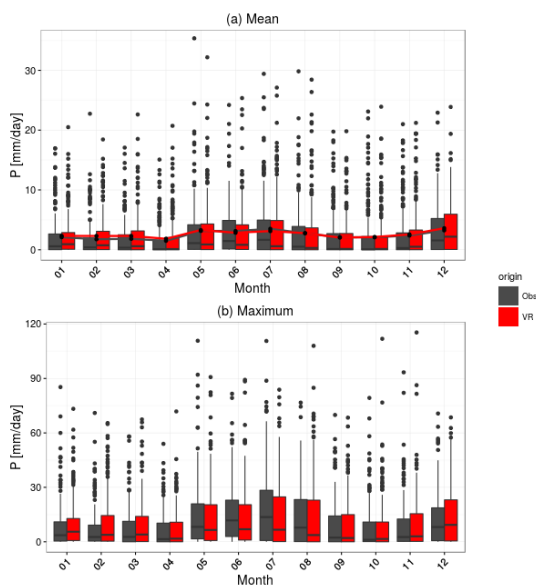
845 **Figure 6: (a) Daily precipitation distribution on a monthly basis as observed (black) and simulated (red). The gray and red lines**
846 **indicate the monthly mean precipitation. (b) Maximum daily precipitation for the given months for the 71 DWD stations and the**
847 **corresponding simulation. Box sizes as explained in the caption of Figure 10.**

848

849

851
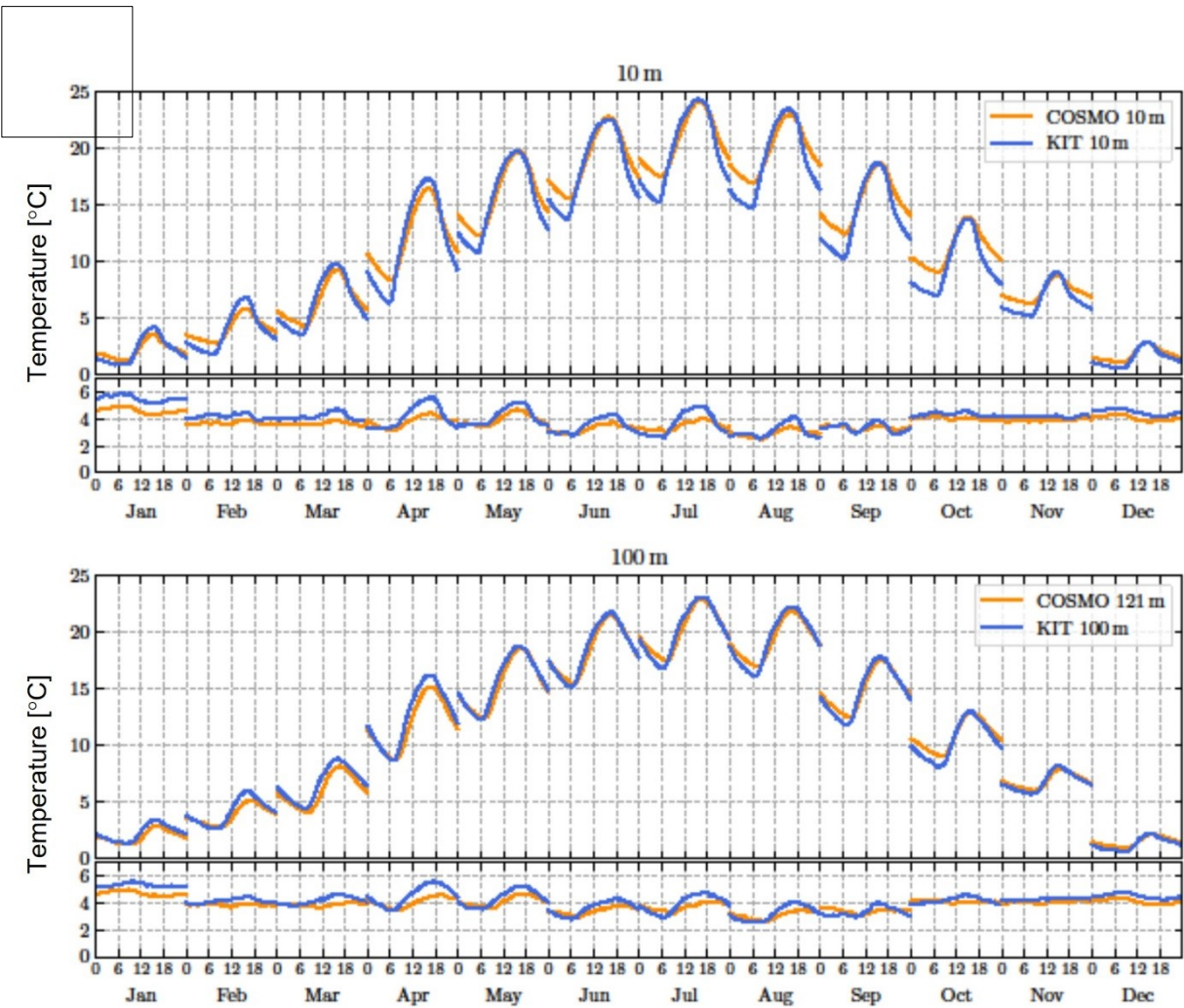
Figure 7: Monthly mean diurnal cycles (local time) and respective standard deviation (see text) for air temperature [°C] in 10 m (top) and 100 m (bottom) height at the KIT tower and for the COSMO grid boxes around the KIT location.

854
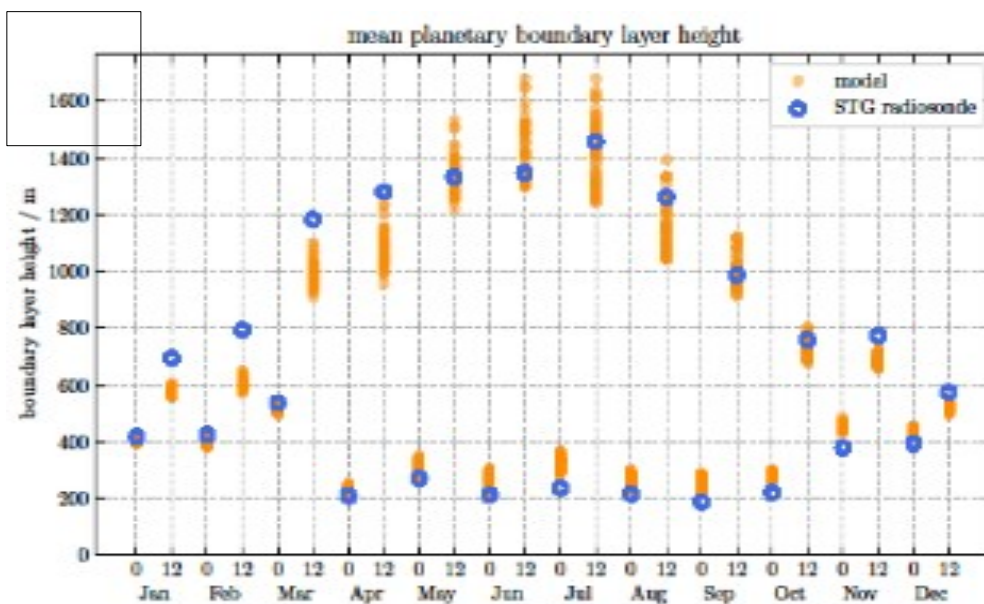
Figure 8: Monthly mean boundary layer height at 0 h and 12 h local time for different land covers diagnosed from radiosonde observations at Stuttgart STG and from atmospheric profiles above grid boxes of CLM.

857
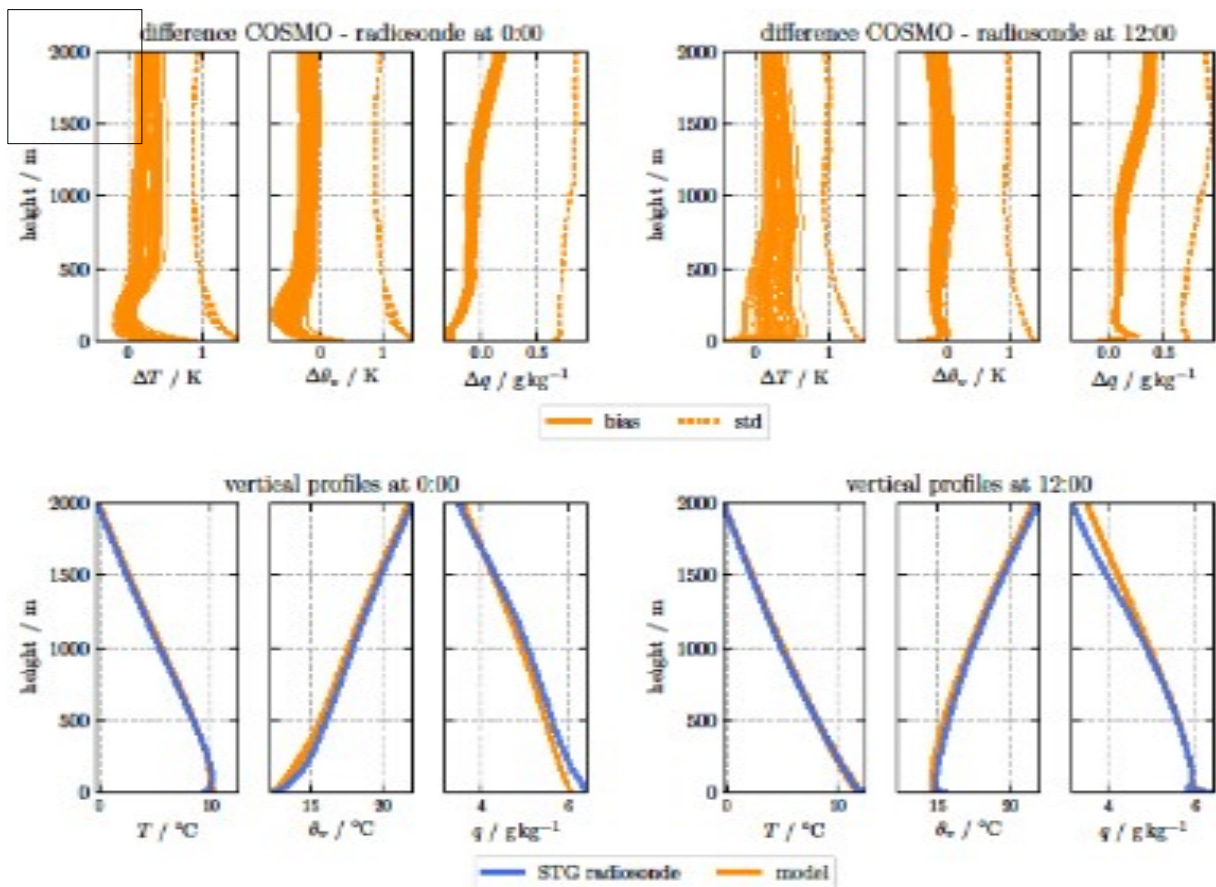
Figure 9: Mean vertical profiles of temperature, virtual potential temperature, and specific humidity (top), and mean differences between modelled and observed data including the standard deviation of the differences (bottom). The experimental data are from the radiosonde data at STG and the simulated data from the grid boxes of the simulated catchment with different land cover (left: 0 h local time, right: 12 h local time).
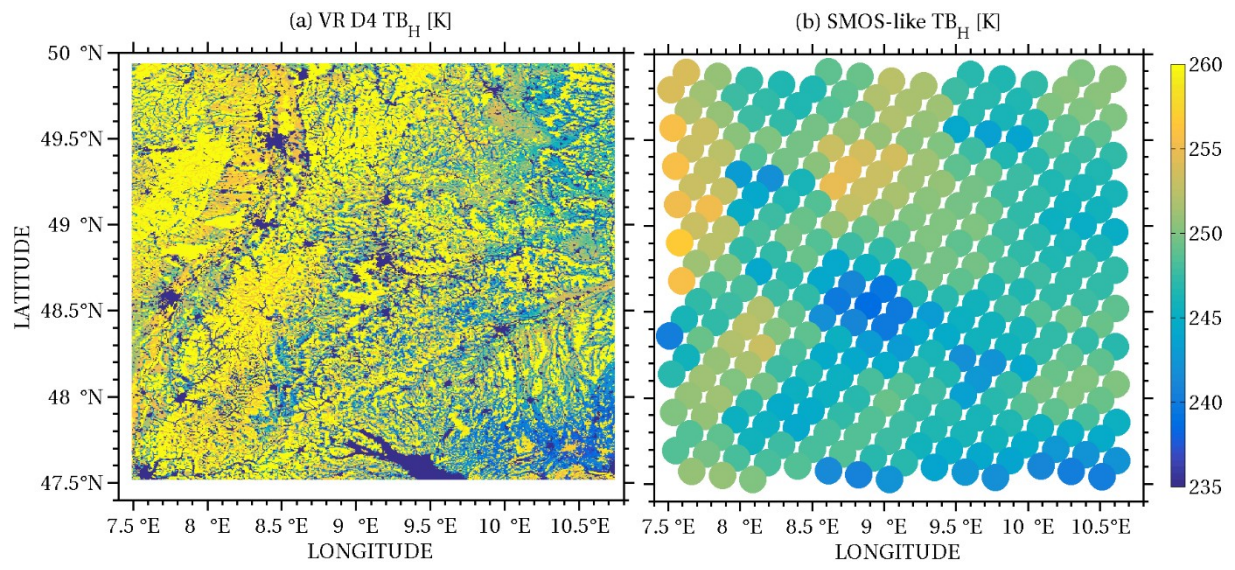
862

863

864 **Figure 10: Area-averaged L-band brightness temperature the period from April to September 2011 for an incidence angle of 30°**
865 **(top) and 40° (bottom). The boxplots indicate the real SMOS observations averaged over the same domain. The black line is the**
866 **median of the observations simulated with CMEM. The dark-gray area corresponds to the inter-quartile range (IQR) while the**
867 **light-gray area encompasses the 3 to 97% range. The orange continuous line indicates the brightness temperature without taking**
868 **into account an assumed bias in surface soil moisture content (see text).**

869
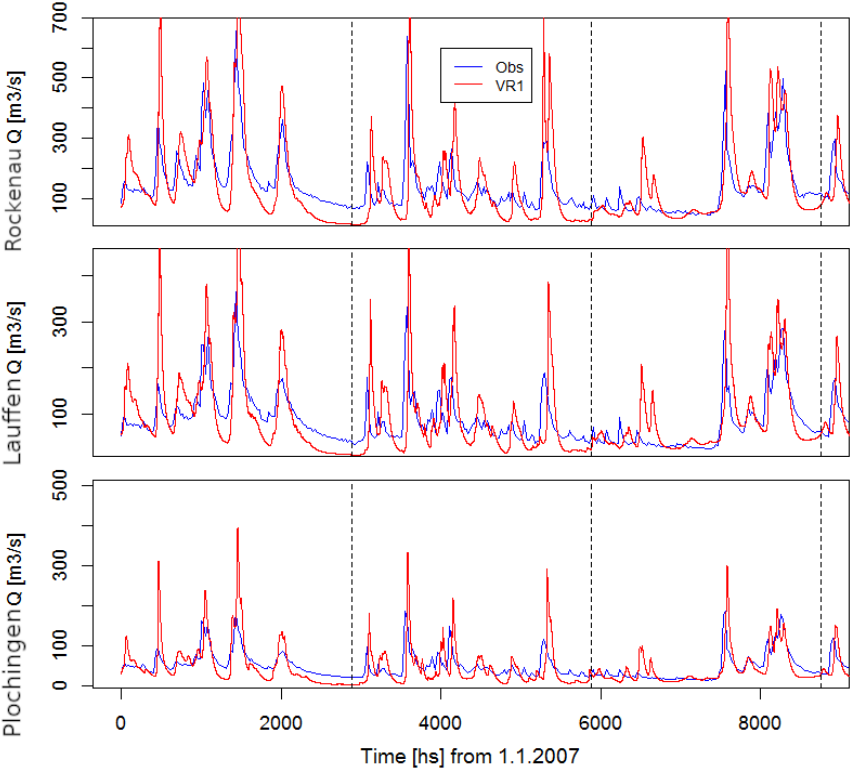
870 **Figure 11: Hourly values river discharge at the gauging stations Rockenau (P1), Lauffen (P2) and Plochingen (P3) for the year**
871 **2007. Blue: observed; red: simulated catchment.**

872

873
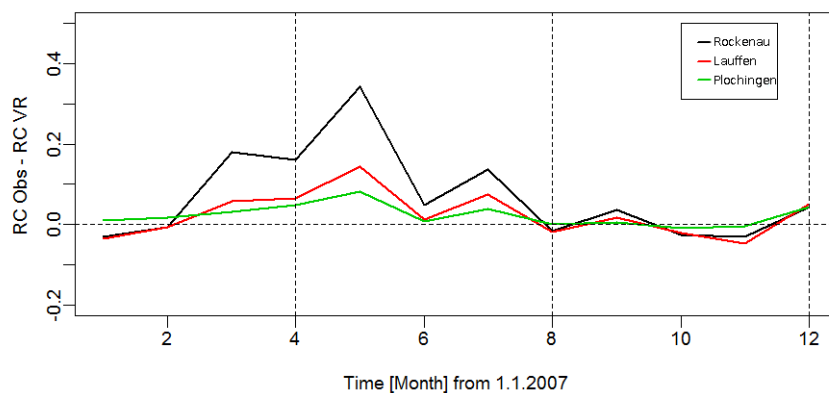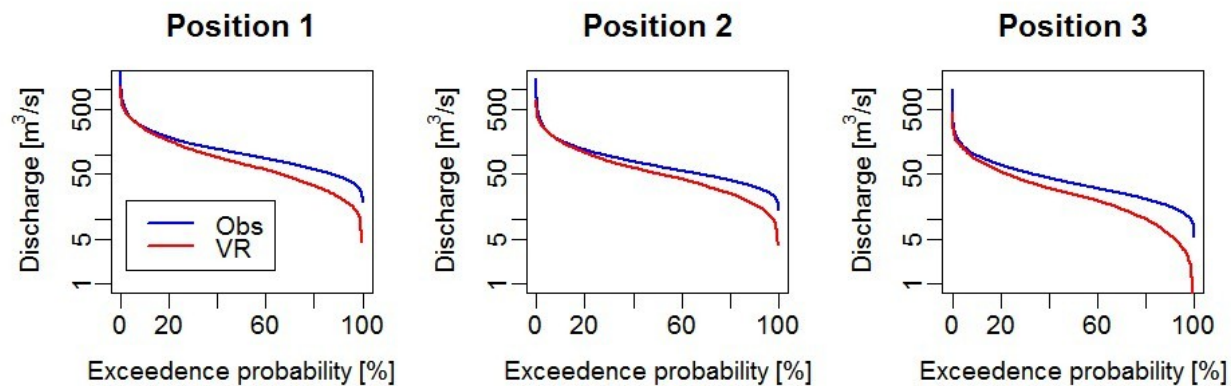
Figure 12: Differences between the run off coefficient calculated for the three stations for the year 2007 based on observations and simulation.

876

877
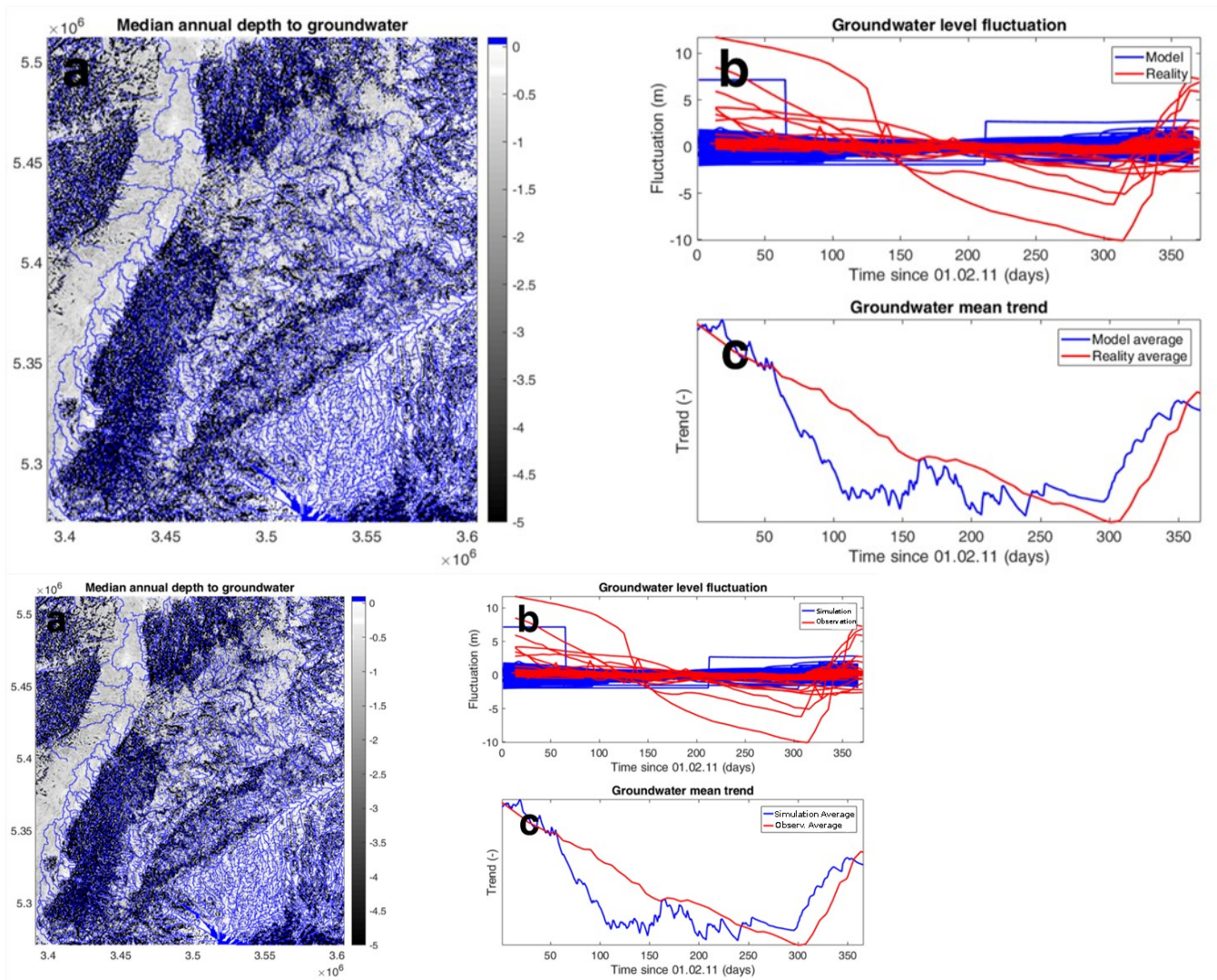
Figure 13:(a) Mean groundwater table depth of the entire domain for the year ranging from 01.02.11 to 01.02.12, (b) groundwater fluctuations around a zero mean and (c) the total mean of all model cells and all real data points superimposed on top of each other to show the annual average trend. Please note that for readability of the figure, subfigure (a) is limited to a maximum depth of -5 m, while the underlying data ranged down to -88 m

882

883

884

885

886

887

888 **Appendix**

889 **7.1 Appendix Tables**

890 **Table A1: Values of porosity and hydraulic conductivity of rocks found in Baden-Wuerttemberg**

Nr.	rock type	Ksat [m/h]	porosity fraction
1	Quarternary	0.00100	0.3
2	Tertiary	0.00100	0.3
3	Upper Jura	0.00720	0.3
4	Middle Jura	10^{-7}	0.3
5	Lower Jura	10^{-7}	0.3
6	Upper Triassic (Keuper)	0.00036	0.3
7	Middle Triassic (Muschelkalk)	0.00180	0.3
8	Lower Triassic (Buntsandstein)	0.02160	0.4
9	Upper Permian (Rotliegendes)	0.00360	0.3
10	New Red Conglomerate	0.00100	0.3
11	Bedrock/Granite	10^{-7}	0.3

891

892

893

Table A2: Observed atmospheric variables at KIT and STG. Local time at STG is UTC+01.

895

dataset	quantity	temporal resolution	height above ground	data coverage
KIT	temperature	10 min averages (resampled to 15 min)	10 m, 100 m	01/2007 – 12/2013
	Incoming and outgoing shortwave radiation		-	
	Incoming and outgoing longwave radiation		-	06/2011 – 12/2013
STG	temperature	12 h (11:45 h and 23:45 h local time)	vertical profiles (interpolated to model levels)	01/2007 – 12/2013
	dew point temperature			
	pressure			
	incoming shortwave radiation	1 h averages	-	
	incoming longwave radiation		-	

896
897
898

899 **Table A3: Strengths and Weaknesses of our simulation regarding several variables**

Variable	Strength	Weakness	Other comment
River discharge	Adequadely captures flood events	Underestimated base flow	Could be improved by higher resolution of the river cells (ParFlow in general)
ET	Shows expected behavior	Little variability in forests as they are never water limited	-
Precipitation	Good agreement with observations in general	Some specific areas show larger differences	Could be fixed by larger simulation area and new parametrizations for the 1km scale
ABL representation	Good fit to tower and radiosonde observations, especially during the daytime in summer	Overestimated nighttime temperature, especially in the summer	Related to COSMO parametrization of near surface inversion at night
Groundwater dynamics	Dynamics closely resembles measured dynamics	Absolute values are biased	Could be related to our simplification of not considering karst
Large-scale soil moisture (satellite)	Dynamics throughout the year are captured well	Large bias in absolute values	

900
901

7.2   Appendix Figures

903
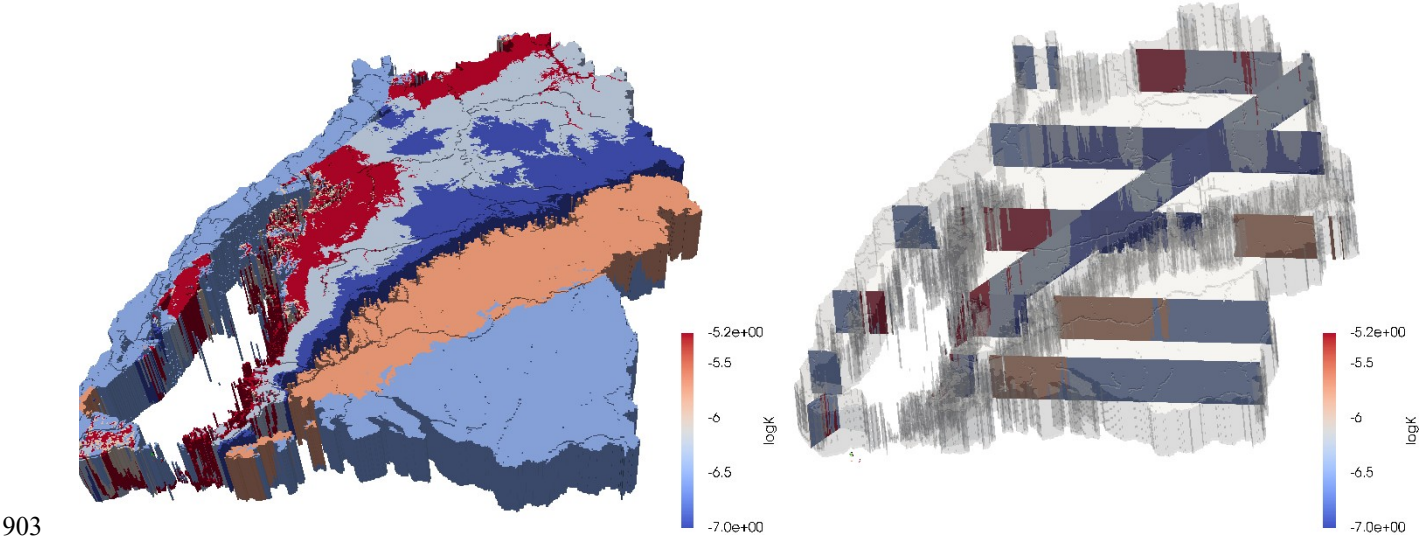
Figure A1: Stratigraphy in the state of Baden-Württemberg represented by its logarithmic conductivity. The left figure shows a 3-D view of the 100 m deep geological model used in this work, where the elevation has been neglected for readability and the transparent regions corresponds to low-permeable material. The right figure shows the same using cross-sections to better visualize the vertical heterogeneity.
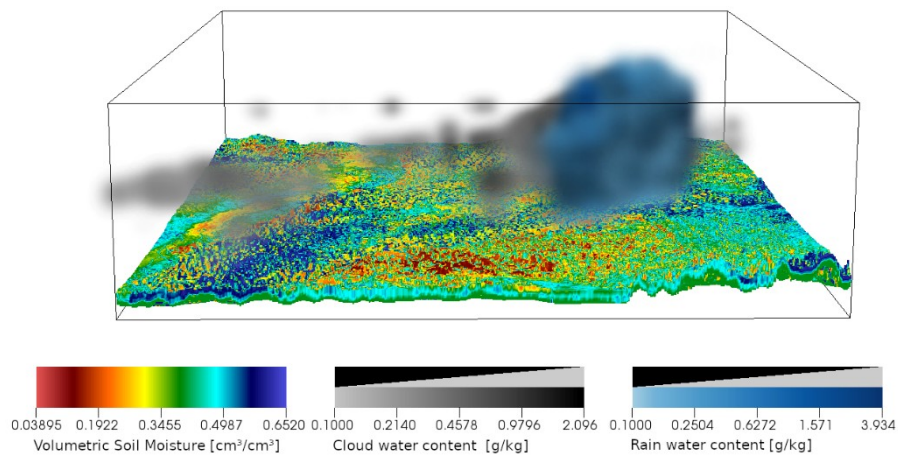
908
909 **Figure A2: Snapshot of the three dimensional distribution of cloud water/ice [g/kg] (greyscale), precipitation/rain water [g/kg]**
910 **(blue in foreground over cloud) and soil moisture [cm3/cm3] (colored) at a time point with a single rain cloud with light rain.**
911

912
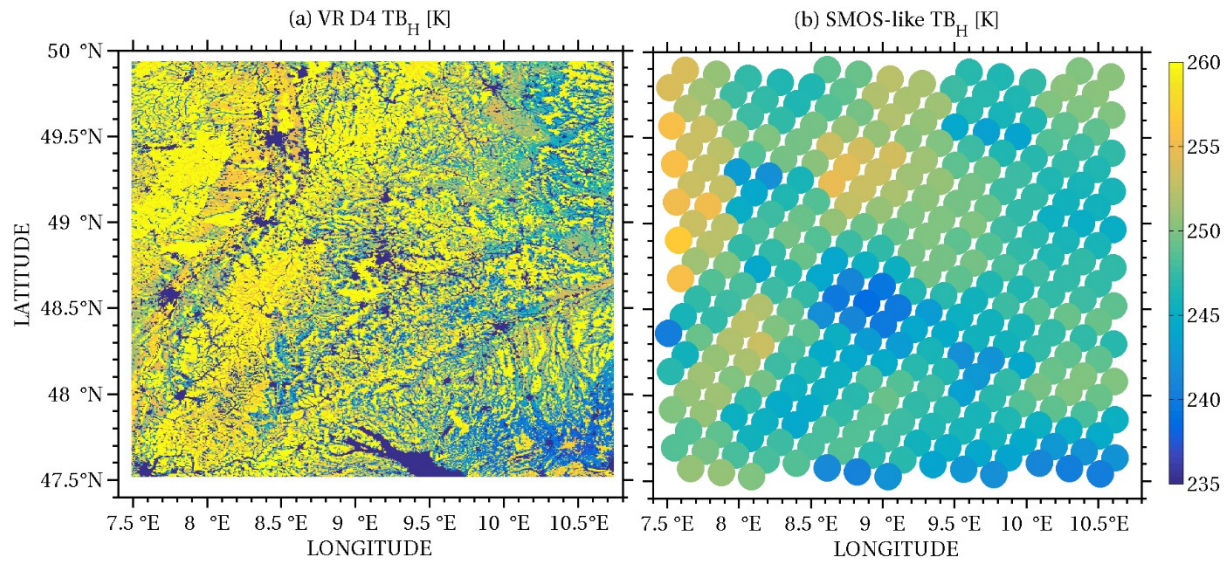
Figure A3: Brightness temperature calculated by the application of CMEM (H-polarization) on the simulated-reality output on July 2nd 2011 (left) and its aggregation on the spatial resolution of the L1C data-product SMOS passive microwave radiometer (right).

916
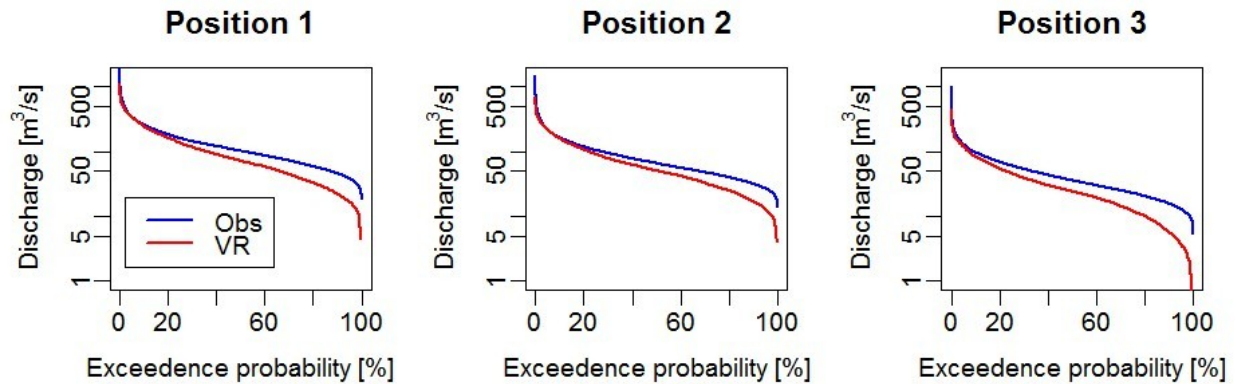
Figure A4: Flow duration curve for the three stations for the three-year time period based on. Blue: observations; red: simulated catchment.

919